First measurement of near threshold J/ψ photoproduction*

Eugene Chudakov, Sean Dobbs, and Lubomir Pentchev

(GlueX Collaboration)

(Dated: March 14, 2019)

Abstract

We report on the measurements of the J/ψ photoproduction cross-section ($\gamma p \to J/\psi p$) in a photon energy range from the threshold of 8.2 up to 11.8 GeV from the GlueX experiment using tagged photon beam produced by the 12 GeV Jefferson Lab accelerator. This energy range was poorly covered by previous old experiments, while our measurements are the first that extend close to the threshold. The near threshold photoproduction of J/ψ has recently gained significant interest due to the expectation of the LHCb pentaquarks ($P_c^+(4380)$ and $P_c^+(4450)$) being produced in the s-channel of the reaction. An upper limit on the $P_c^+(4450) \to J/\psi p$ branching fraction is estimated. The measured cross-sections are compared with theoretical predictions and threshold production mechanisms are also discussed.

* Thanks to everybody who contributed to this work

CONTENTS

I. GENERAL REMARKS

The upgraded 12 Gev JLab accelerator provides a unique opportunity (correct energy, high intensity, and polarized beams) to study the J/ψ photoproduction right above the threshold (at beam energy of $E_\gamma = 8.2$ GeV) up to the maximum energy. Hall D is the only hall to which a beam of energy higher than 11 GeV can be delivered. Reaching the maximum beam energy is very important in order to allow comparison to the higher energy measurements at SLAC, which start at 13 GeV. In the spring of 2016 the maximum tagged photon energy was 11.85 GeV, while for the later running it was lowered to 11.4 GeV. Therefore, the 2016 data is the only one so far (and will remain the only for several more years) that can give valuable information in the high energy region next to the SLAC measurements. Given the history of the differences in the flux normalized yields in 2016 compared to those in the following years, it is important to have a procedure that allows to check the normalization for the different periods of running.

We study the exclusive reaction:

$$\gamma p \to p e^+ e^- \tag{1}$$

in the region of the e^+e^- invariant masses, $M(e^+e^-)$, above 0.9 GeV, that includes ϕ, J/ψ, as well as the Bethe-Heitler (BH) process as a continuum. We use BH in the invariant mass region of $1.2 - 2.5$ GeV for the absolute normalization of the J/ψ total cross-section, thus eliminating uncertainties from factors like luminosity and common detector efficiencies. The BH e.m. diagrams can be calculated exactly in principle. In fact, there are close-to-singularity (limited only by the electron mass in the propagator) kinematic regions that can cause numerical problems. However these regions are excluded, mostly by the detector acceptance and also by additional fiducial cuts in the analysis.

For illustration, we show in advance in Fig.1 the invariant mass spectrum from the data compared to Monte Carlo (MC) simulations as described later in details. In contrast to the J/ψ and ϕ narrow peaks for which the signal can be separated from the background, the BH continuum is contaminated with pions. Compared to the electrons, the pions are orders of

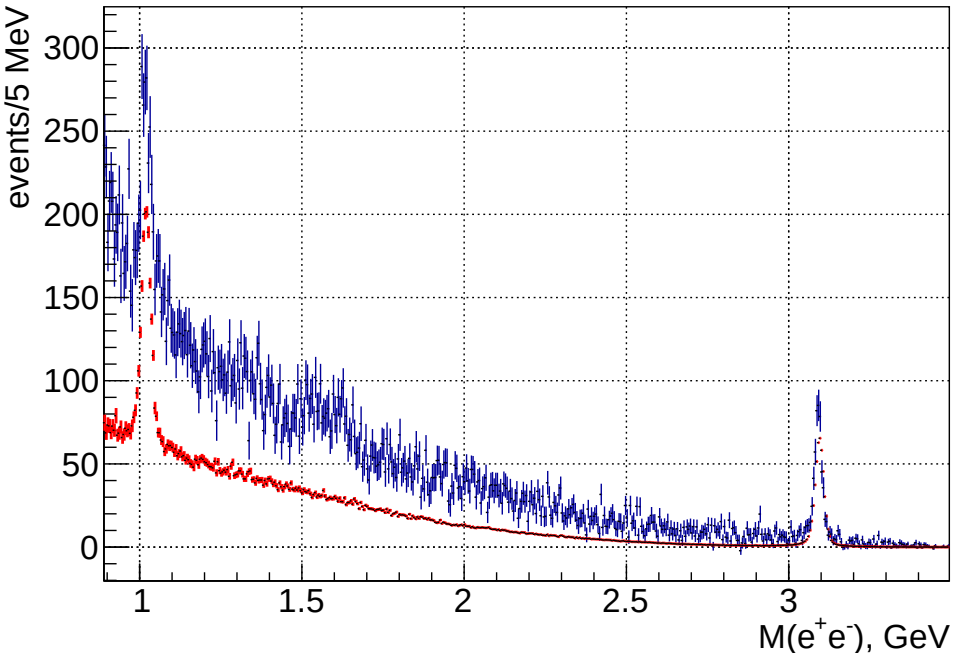

FIG. 1: $M(e^+e^-)$ invariant mass spectrum – simulations (red) vs data (blue)

magnitude more numerous for which the GlueX experiment doesn't have enough rejection power to reduce their number to a negligible level. We estimate the pion background from the p/E (momentum p from the tracking and energy E from calorimetry) distributions and subtract it from the continuum. Despite this drawback, compared to using ϕ for normalization, the BH process has relatively high yield and kinematics that are closer to the J/ψ region which allows to study the detector efficiency and other important systematic effects, as discussed later.

As a cross-check one can aim to estimate the cross-section of the ϕ photoproduction and compare it to the only measurement in this energy range [1]. However, we do not intend to include this in the publication. Due to the much lower ϕ mass the kinematics of this reaction and correspondingly, the detectors involved, are very different from those in the J/ψ photoproduction. Therefore, such comparison relies much more on MC and respectively requires a better understanding of the different detectors.

We discuss the obvious data/MC disagreement in the continuum in Fig.1 as mainly coming from the pion contamination. We take advantage of the exclusiveness of the reaction and use a kinematic fit to reconstruct the momentum components of all final state particles. As a result we reach invariant mass resolutions on the order of $10 - 15$ MeV as seen from

the J/ψ and ϕ peaks. Note that all the quantities discussed in this paper are the results of the kinematic fit unless otherwise stated. An important exception of this rule is the use of the missing mass off the recoil proton, in which case the measured proton momentum and angle are used. Even in this case the kinematic fit is needed to suppress the pions using the p/E cut, where, to have enough resolution, the electron momentum from the kinematic fit is used.

We analyze all the production data from the 2016 and 2017 spring runs. We simulate the J/ψ, as well as the ϕ photoproduction and the BH process. Technical information about the data set and the software version used for reconstruction and analysis both of the data and generated events can found at the end of the paper.

II. DATA RECONSTRUCTION

The data reconstruction is done within the standard Hall D framework. The *REST* files produced from latest reconstruction version (August 2018) are analyzed using the standard Hall D analysis library. The plugin (*jpsi_lp*) used for these analysis specifies the exclusive reaction, $\gamma p \rightarrow pe^+e^-$, in the $0.5 < M(e^+e^-) < 4.0$ GeV invariant mass region. Loose pre-selection cuts are used within the plugin to reduce the amount of data. All possible combinations per event that satisfy these cuts are passed (as root trees) to the next custom level of analysis where the final cuts, as discussed through this section, are applied. These specific cuts are mainly needed to suppress the pion background. They are optimized using the BH process, as it will be used for normalization. We aim to use only those cuts that are absolutely necessary and can be reliably simulated.

The events generated to simulate a particular process are passed to the Hall D detector simulator based on Geant 3 package. This procedure is done using the standardized *MCWrapper*. For each running period the simulated runs are mixed proportionally to the number of triggers taken in each real run. For each run, "random hits", taken from the data with a pulser trigger are injected at the hit level into the generated events. The tagger accidentals are simulated in a similar way. The runs that do not have such random hit information are excluded from the simulations. In 2016 the two low priority run blocks (runs 10391-11300) are not used, while there are only several such runs from 2017. The input photon energy is taken from the measured beam spectrum for the corresponding running period. The simulations produce *REST* files that are analyzed in exactly the same way as the data.

Technical details about the data set, software versions of the reconstruction, production, and analysis, as well as full list of the cuts used in the analysis are summarized in Appendix, Section VII.

A. Event pre-selection

Here we describe the modifications to the standard cuts found in the analysis library. We loosen the timing cuts for all the detectors and particle types (see Table XII). We also loosen the cut on the missing mass squared: $-0.25 < M^2_{miss} < 0.25$ GeV^2, compared to ± 0.1 GeV^2 in the standard analysis. On the other hand, we apply an additional cut on the missing transverse momentum $p_{Tmiss} < 0.5$ GeV. The plugin requires a kinematic fit with both 4-momentum and vertex constraints. A loose cut on the kinematic fit $\chi^2 < 5000$ (the number of degrees of freedom is 7 for this reaction) is applied. Finally, for the electrons and positrons we require $E/p > 0.7$ (the momentum is taken from the kinematic fit) which significantly reduces the amount of data. There are very loose requirements about limiting the number of unused tracks per event. The problem with a tighter cut is that it is difficult to predict the percentage of the bogus and split tracks and such a cut would reduce the efficiency by an amount that is very difficult to simulate. However, due to the p_{Tmiss} and M^2_{miss} cuts the real extra tracks are suppressed, as estimated later.

B. Electron/positron identification

The cuts on different variables described here have been studied in an iterative way. Here we show the final results. If a variable is plotted, it means that all the other cuts have been applied (as described one-by-one in this section and in the Appendix), except the ones on the plotted variable. An exception of this rule is for pions as explained below.

1. p/E cuts

The pions are suppressed mainly by applying a p/E cut for both, electron and positron candidates, using the energy measured from FCAL and/or BCAL and the momentum from the kinematic fit. We quantify the cut value by N_σ, the number of R.M.S., σ, from the mean value, $\langle p/E \rangle$. Thus, electrons can be identified by requiring:

$$p/E < \langle p/E \rangle + N_\sigma \sigma \tag{2}$$

To separate the background, first we study the response of the calorimeters to pions. We

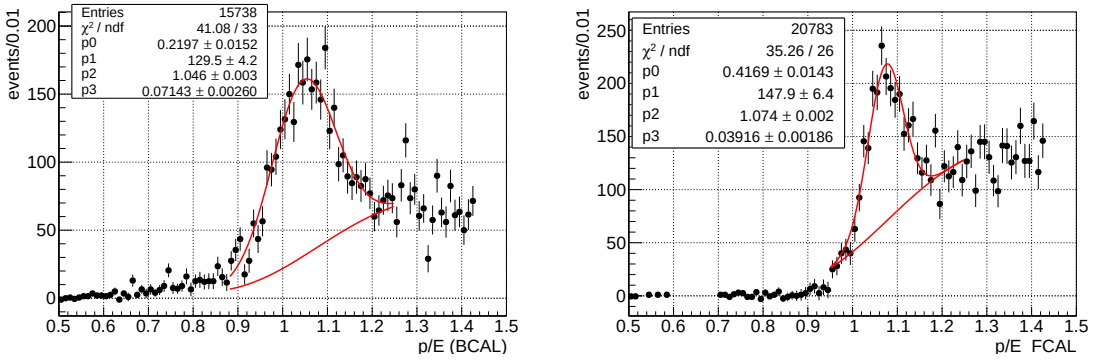

(a) BCAL (b) FCAL

FIG. 2: p/E distributions for BCAL/FCAL obtained by applying 0σ cut on the other lepton. First parameter is a normalization for the pion background shape, while the other three are for the Gaussian. The background (bottom) and the total (top) are shown with separate curves.

create a pion sample by applying 3σ anti-electron cut ($p/E > \langle p/E \rangle + 3\sigma$) for one of the lepton candidates (keeping all the other cuts the same) and look at the p/E distribution of the other one. We parametrize the shape of this background distribution with a 5th order polynomial. In order to obtain a cleaner electron sample we apply a tight (0σ) electron cut on one of the leptons and analyze the p/E distribution of the other one. We fit this distribution with the background shape (multiplied by a normalization parameter) summed a Gaussian.

This procedure is illustrated separately for the BCAL and FCAL in Fig.2. For these studies we use an invariant mass range of $1.2 - 2.5$ GeV. Based on the widths of the J/ψ and ϕ peaks in Fig.1, we conclude that the resolution of the lepton momenta, as coming from the kinematic fit, is better than 1%, therefore the main contribution to the widths of the p/E distributions in Fig.2 comes from the calorimeter resolution. However, additional contribution may come from electron radiation. The kinematic fit tries to correct the measured electron momentum to its initial value before the radiation, while the calorimeters measure the final energy. Thus, BCAL/FCAL have effective (i.e. including radiation effects) resolutions of about 7%/4% respestectively, both being off from unity. Thus, in the following analysis, to separate the electrons/positrons we apply 2σ cuts on both leptons with mean and R.M.S. values as obtained from the above fits, separately for BCAL and FCAL. In MC we smear and shift the BCAL and FCAL energies to match the results on these plots. Therefore, we apply the same cuts to both data and MC. Table I summarizes these results.

Calorimeter/data type	$\langle p/E \rangle$	σ	2σ cut
BCAL data	1.0462	0.0683	1.1827
BCAL MC	1.0290	0.0466	1.1827
FCAL data	1.0738	0.0392	1.1521
FCAL MC	1.0135	0.0271	1.1521

TABLE I: p/E mean, R.M.S. and cuts for the data and MC and the two calorimeters. Note: before applying the cuts, MC is smeared and shifted to match the data.

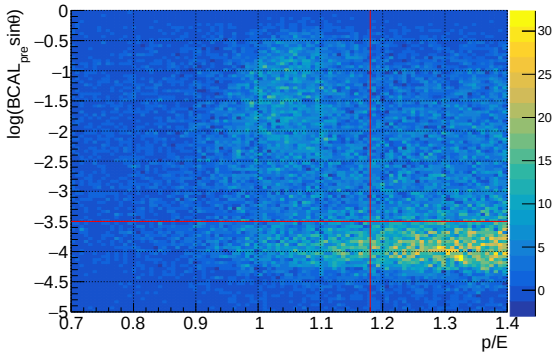

FIG. 3: Logarithm of $BCAL_{pre} \sin\theta$ vs p/E from BCAL pre-shower ($BCAL_{pre}$) and shower (E) signals. Cut on $BCAL_{pre} \sin\theta > 0.03 = e^{-3.5}$ GeV and the standard high p/E cut are shown as red lines.

2. BCAL pre-shower cuts

The innermost BCAL layer is used as a pre-shower detector, allowing further suppression of the pions. Fig.3 illustrates this, where the logarithm of the pre-shower signal ($BCAL_{pre}$) times $\sin\theta$ (θ is the lab polar angle) is plotted against p/E. The $\sin\theta$ term is needed to take into account the geometrical thickness of the inner layer along the shower path. One can see that by applying in addition a pre-shower cut as $BCAL_{pre} \sin\theta > 0.03$ GeV, significant fraction of the pions are removed (lower left quadrant on the plot). Fig.4 compares the pre-shower signal distributions from the data in the BH and J/ψ regions with the corresponding MC for the signal. One can see the agreement between data and MC and that the low cut is safe enough removing only about 2% of the signal.

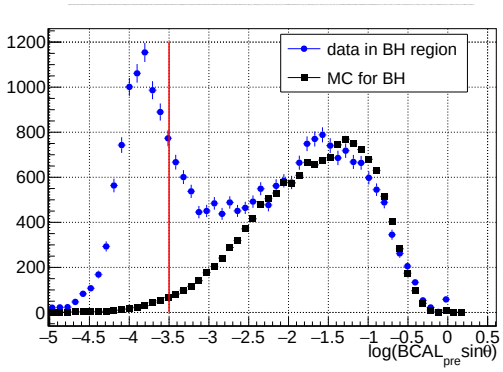

(a) In the BH region of $1.2 < M(e^+e^-) < 2.5$ GeV.

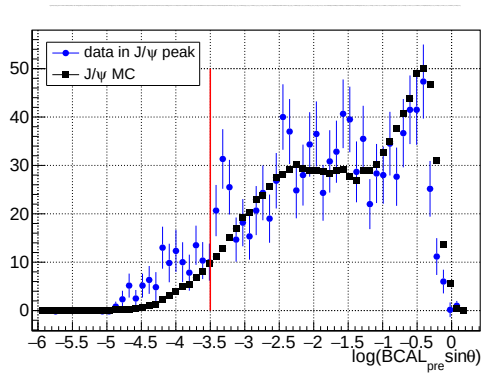

(b) For the J/ψ peak.

FIG. 4: Distribution of the BCAL pre-shower signal (same as on Fig.3) – data compared to MC – for BH and J/ψ. The red line represents the low cut position.

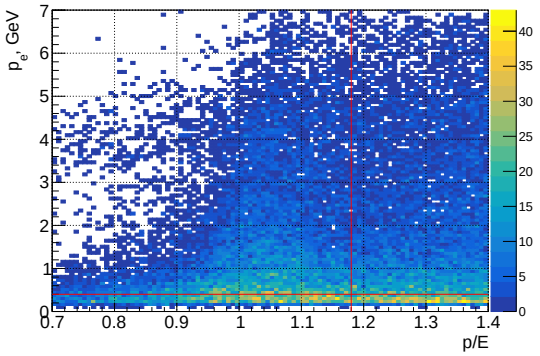

FIG. 5: Electron/positron momentum vs p/E from BCAL. Low cut for p_e and high cut for p/E are shown with red lines.

3. Fiducial cuts

These cuts are applied directly to the kinematic fit quantities for which we are confident better match the simulations. We require both electron and positron momenta to be greater than 0.4 GeV. As seen from Fig.5, this requirement cuts low momenta pions in the BCAL originating mainly from target excitation. We verified that this cut is superior over a cut that excludes the production of Δ^{++} and Δ^0 (1.232 $\pm$0.1 GeV) which we reconstructed as the invariant mass of pe^+ and pe^- respectively, with replacement of the electron mass by the pion one. We prefer the momentum cut due to its simplicity and reliable simulation. In addition we require the polar angles of the electron and positron to be greater than 2° which eliminates bogus tracks originating from electromagnetic background hits in the FDC close

variable	units	lower limit	upper limit
p_e	GeV	0.4	no limit
θ_e	deg	2	no limit

TABLE II: Fiducial cuts.

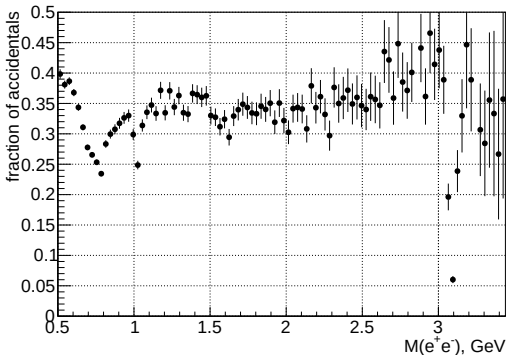

FIG. 6: Fraction of the accidental combinations for the whole set of 2016 and 2017 data with all cuts applied, as function of the invariant mass.

to the beam line. The fiducial cuts are summarized in Table II.

4. CDC dE/dx for electrons/positrons NOT used in the analysis

One important cut that allows the suppression of the pions, the cut on the energy losses dE/dx in the CDC, was not used in this analysis. In the different reconstruction versions and run periods different quantities from the data were used to calculate dE/dx - the integral (total charge) or just the amplitude of the first peak as seen by the fADC125. Both methods have issues in estimating dE/dx, as it exhibits dependence on the track angle w.r.t. the wire. This is due to space charge effects that are very strong when the track is perpendicular to the wire ($\theta = 90^0$), but are still noticeable down to $\theta = 30^0$. The reliable simulation of such an effect is questionable, to say the least. The effect may also vary from run to run. The dE/dx cut would help only for momenta ~ 0.4 GeV, i.e. around the pion ionizing minimum, which introduces additional selectivity that is difficult to simulate. Thus, such cut was not used.

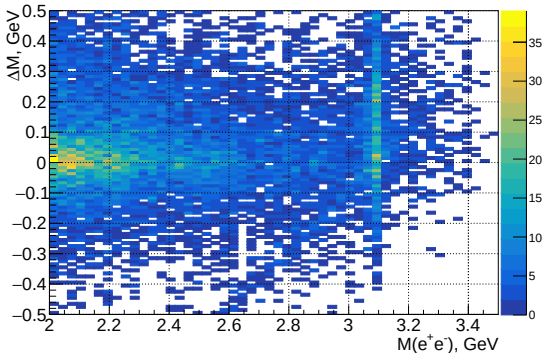

(a) Difference between the invariant masses of a given combination and all the other combination vs the invariant mass of that combination if it is within the correct beam bunch. Single combination events are excluded. Note the 45° band that crosses zero at the J/ψ invariant mass, that comes from the in-time accidentals.

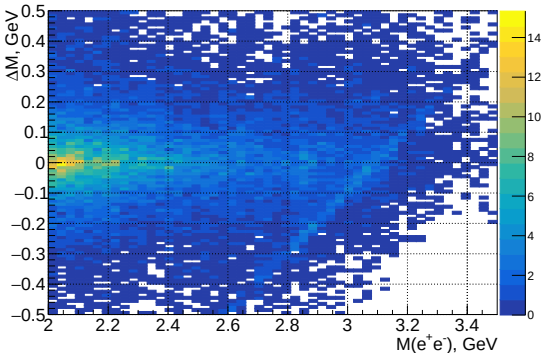

(b) Same as in Fig.7a but for out-of-time combinations weighted accordingly. Note the 45° band that comes from the out-of-time accidentals.

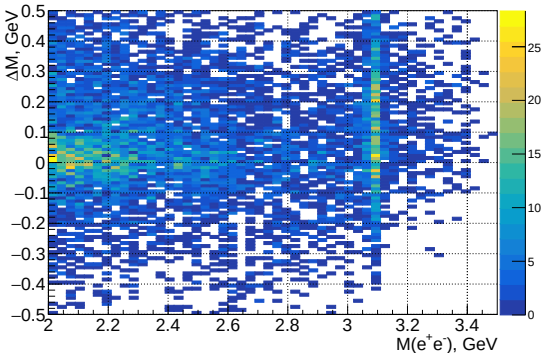

(c) The difference between the histograms of Figs.7a and 7b. Note the 45° band disappears.

FIG. 7

C. Accidental and combinatorial background

Within an event, we distinguish two types of combinations, the ones that have different tagger energy and combinations with the same tagger energy but different track hypothesis. Our analysis code counts event-by-event the multiplicity of both types.

We save information from three beam bunches on each side of the in-time-peak. The energy combinations that have used the wrong photon energy are also accidental in time. For each quantity that is being analyzed we subtract the accidentals statistically using the

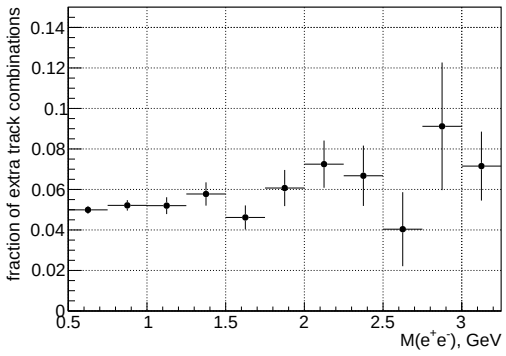

(a) Fraction of extra (multiple counting) track combinations over the total number of events.

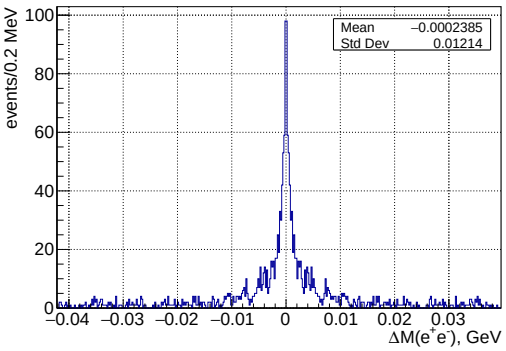

(b) Within an event, difference between invariant masses for different track combinations. Single combination events are excluded.

out-of-time combinations. Fig.6 shows the fraction of accidental combinations as a function of the invariant mass. On average, for the whole set of data it is $\sim 35\%$ in the continuum region and drops to 6% at the J/ψ peak. The Figs.7a,7b,7c demonstrate that indeed this procedure removes the wrong energy combinations. Plotted on the three figures is the difference between the invariant masses of all energy combinations within one event, vs the invariant mass, respectively for the in-time, out-of-time (weighted appropriately by a factor of 1/6) combinations, and their difference. One can see that the band that is created from the J/ψ events when using wrong energy, is removed in the difference plot.

The track combinations are not accidental and may come for example from swapping two tracks (like proton and positron) or from track splitting. Our study shows that after applying all the cuts the fraction of the extra combinations (i.e. same event counted multiple times) is $\sim 5-7\%$, see Fig.8a. Moreover, Fig.8b shows that the invariant mass difference within one event of such combinations is mostly within several MeV. In the BH and J/ψ analysis we count the extra combinations bin-by-bin in t or beam energy and subtract them from the total yield.

variable	units	lower limit	upper limit
$M(e^+e^-)$	GeV	1.2	2.5
p_p(for E_γ studies)	GeV	0.4	–
$-(t-t_{min})$ (for E_γ studies)	GeV^2	0	0.6
E_γ (for t studies)	GeV	10	11.8

TABLE III: Additional cuts applies for the BH process.

III. BETHE-HEITLER PROCESS

We study the beam energy, E_γ, and the t dependence of the BH process in the $1.2 < M(e^+e^-) < 2.5GeV$ invariant mass region which will be used for the J/ψ cross-section normalization. We apply additional fiducial cut on the proton momentum of $p_p > 0.4$ GeV, to exclude the region where the proton is poorly reconstructed. This cut is needed only for low invariant masses; it's irrelevant for J/ψ where the minimum proton momentum is 0.6 GeV. The cut is also not used when studying the t-dependence because of the direct t - p_p relation. As it will be clear in this section, when studying the E_γ-dependence we apply a cut to avoid the high-t region where the pions dominate. At the same time when we study the t-dependence we are interested in the high energy part of the beam spectrum as discussed in the next section. These additional cuts that are applied for the BH process (unless otherwise noted) are summarized in Table III.

A. Bethe-Heitler simulations

We rely on the BH generators to calculate the absolute cross-section in the continuum that will be used for normalization of the J/ψ cross-section. Therefore, for more confidence, we have used two independent generators that use completely different methods of calculating the BH cross-section. The first one, that we will call "Hall B" [2] is based on analytical calculations [3]. The second one, "Hall D" [4] calculates the Feynman diagrams numerically. Both methods have to deal with close-to-singularity kinematic regions limited only by the electron mass in the propagators, which requires much higher statistics in these regions. The Hall B generator uses flat but variable phase space range, which helps to extend the

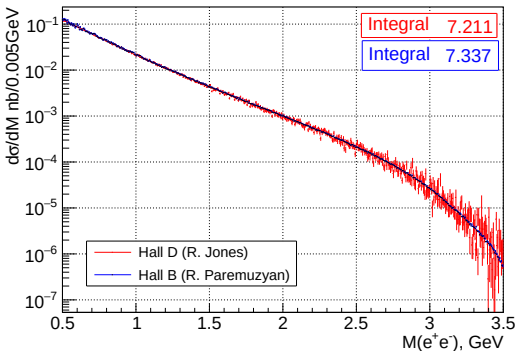

(a) Invariant mass spectrum from the two BH generators for $-(t-t_{min}) < 0.6$ GeV^2. The integrals represent corresponding total cross-sections in nb.

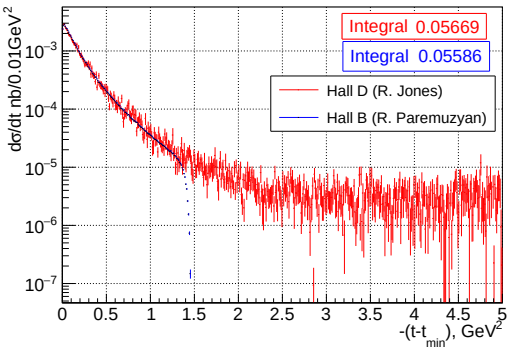

(b) $d\sigma/dt$ from the two BH generators for the $2 < M(e^+e^-) < 2.5GeV$ region. The integrals represent corresponding total cross-sections in nb.

FIG. 9

limits where the cross-section can be reliably calculated. There are additional constraints in the analytical calculations [3] that for example limit the t-region up to maximum 1.5 GeV^2. Other constraints have to be applied on the angle θ_{CM} defined as the polar angle of the electron in the e^+e^- CM frame, with the z-axis being opposite to the proton direction. In the Hall D generator a weighted phase space is used allowing the calculation of the total BH cross-section. Still, for very forward kinematic it requires significantly higher statistics.

In this subsection we will apply only the fiducial cuts defined in Table II and the specific BH cuts in Table III depending on the variable being studied. In fact, for the final cross-section normalization all the cuts are important, however, for the purpose of comparing the generators we will use only the fiducial cuts. The first two cuts, on p_e and θ_e, exclude the region where the cross-section rapidly increases which is the source of the numerical problems discussed above.

In Figs.9,10 we compare the results from the two generators for $M(e^+e^-)$, $t-t_{min}$, and beam energy. Given the completely different method of calculations, the agreement between the two generators is amazing, at the level of 2% which is consistent with the statistical error. This also means that the fiducial cuts satisfy the constraints in θ_{CM} and t needed for the Hall B model. One can see in Fig.9b the t-limit of the Hall B generator, which however doesn't affect the results since the high t-region is excluded in the cross-section normalization. The peak at small t Fig.10a is real and is due to the fiducial cuts (Table II) that are applied.

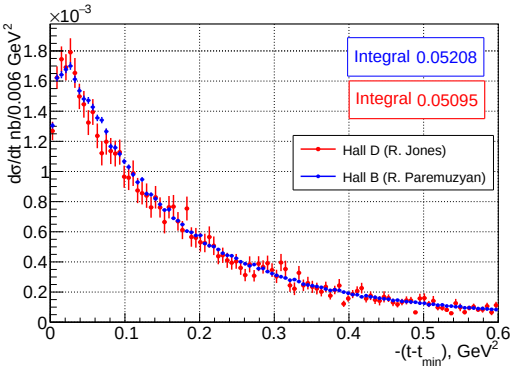

(a) Same as in Fig.9b but for the low t region. The integrals represent corresponding total cross-sections in nb.

.

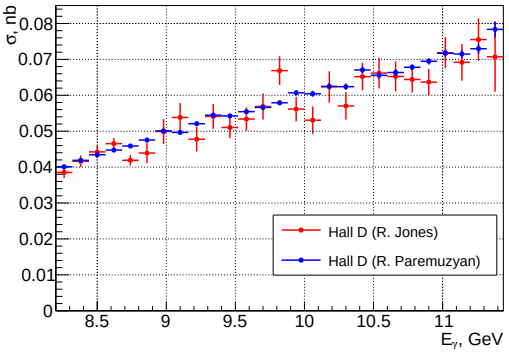

(b) Total cross-section for $-(t-t_{min}) < 0.6$ GeV^2 and $2 < M(e^+e^-) < 2.5$ GeV as function of the beam energy from the two BH generators.

FIG. 10

The BH simulations use the experimental flux distributions, separately for 2016 and 2017, as an input photon spectrum. Unlike the J/ψ simulations, there are no input parameters needed to calculate the BH cross-section.

B. Signal/background separation

The application of the cuts described in the previous section is not enough to eliminate the pion contamination in the continuum region. Therefore, the strategy is to use the p/E distributions to fit the electron peak on the top of the pion background. We will do these studies separately for the BCAL and FCAL due to their different resolution. For illustration, we plot in Fig.11 the p/E distribution of one lepton vs the other if the one on the x-axis is registered in the BCAL/FCAL. Only for this plot we have shifted the mean p/E values for the BCAL and FCAL (see Table I) to unity. The pion contamination has to be studied in bins of beam energy and t. Because of statistics limitations and for simplicity, we prefer to work with one dimensional distributions. In a similar way as for the estimation of the calorimeter resolution, we create a pion sample by applying $2\sigma < p/E < 4\sigma$ cut to one of the lepton candidates (which may be registered either in the BCAL or FCAL) and plot and fit the p/E distribution for the other one, separately for the BCAL and FCAL (blue points in Fig.12).

Next, we apply a $-3\sigma < p/E < 2\sigma$ cut to one of the leptons and plot the p/E distribution

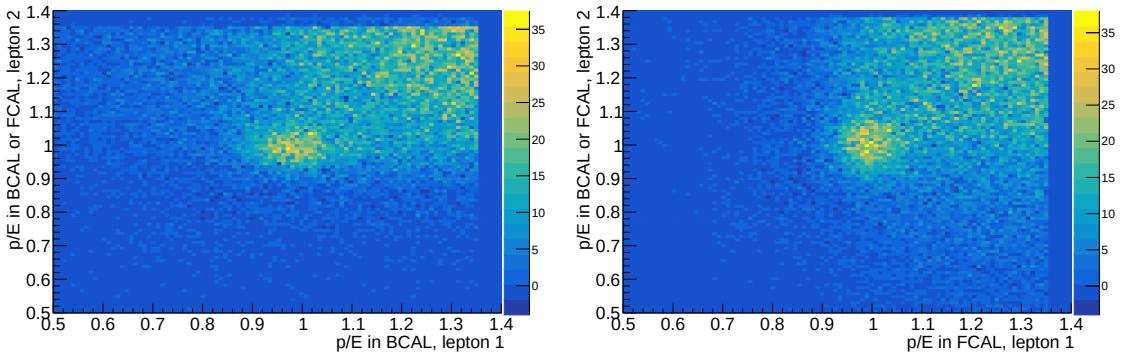

(a) BCAL (b) FCAL

FIG. 11: p/E distribution of the two leptons if the first one is in the BCAL/FCAL

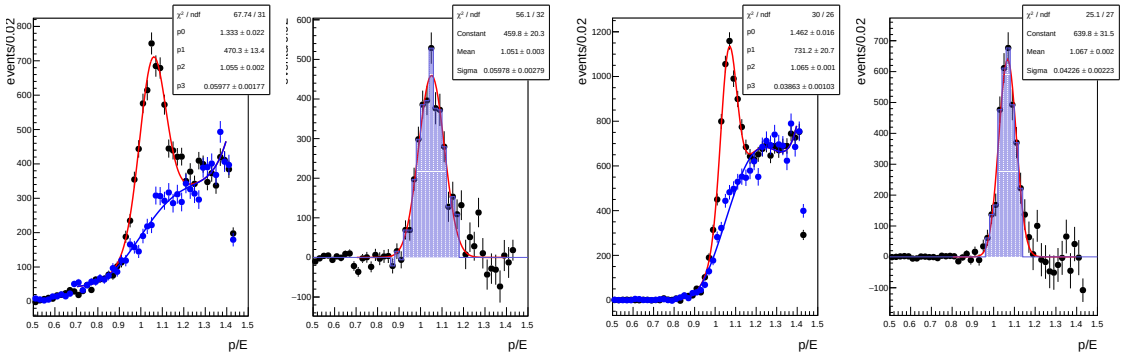

(a) BCAL (b) FCAL

FIG. 12: Right plots in each figure: slices from Fig.11 projected on the x-axis for $2\sigma < p/E < 4\sigma$ cut on the y-axis (blue points) fitted with a polynomial representing the pion background shape and slices from Fig.11 projected on the x-axis for $p/E < 2\sigma$ cut on the y-axis (black points) fitted with the background shape ($p0$ normalization coefficient) and a Gaussian ($p1 - p3$ parameters). Left plots in each figure: the difference of the black and blue points from the left plots (total minus pion background) representing the electron/positron signal fitted with a Gaussian. The shaded histograms represent the events within $-3\sigma/+2\sigma$.

of the other one: black points in Fig.12. Note that before in Fig.2 we have used 0σ electron cuts to create a cleaner electron sample. The distribution is fitted with the pion sample shape times a normalization parameter plus a Gaussian. The signal can be extracted at this stage by integrating the Gaussian (method (I)). To be more accurate, however, we take the difference between the two distributions – the total minus the pion background (right plots in each subfigure in Fig.12) – and either count the number of events (method (II)) or fit and integrate a Gaussian (method (III))within $-3\sigma < p/E < 2\sigma$. We found that the

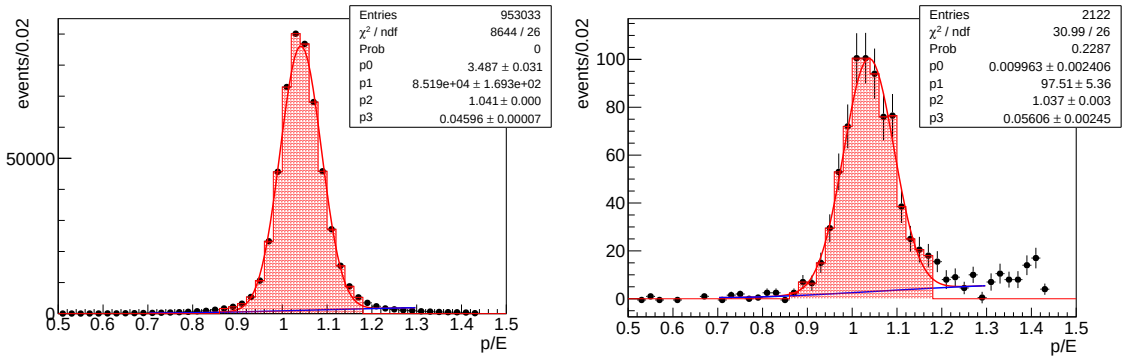

(a) MC (b) data

FIG. 13: p/E distributions in BCAL for the J/ψ peak fitted in the same way as for BH, data and MC

results using this three different methods are consistent. As for the errors, method (I) takes into account the variation of the background percentage as obtained by the total fits, while method (II) includes variations of the background point by point. In any case, the statistical errors for the BH process are much smaller than the statistical errors of the J/ψ signal. For the final analysis we will use method (II). The estimated number of BH events is the sum of the corresponding numbers for the two calorimeters as obtained from the fits, divided by two, due to the fact the each event enters twice (for electrons and positrons) in the p/E distributions. The results in this subsection are for the total distributions. Results in bins of E_γ and t will be presented below. For these fits (due to the low statistics) we have fixed the widths, separately for the BCAL and FCAL (see Table I), of the electron peak.

There was a request by the reviewers to compare the p/E distributions in this subsection with the ones for the J/ψ peak both for data and MC – see Figs.13,14 for the BCAL and FCAL. The widths, both for MC and data, are smaller compared to these in case of BH (Table I) explained by the higher electron/positron energies. Thus the fixed 2σ cut applied on p/E is actually looser in case of J/ψ and safely includes the right tails.

C. Detector efficiency

The detector efficiency is estimated using the BH simulations. The number of reconstructed events with all the cuts applied is divided by the number of the thrown events in bins of beam energy, E_γ, or t. The exact same procedure that is used in data reconstruction

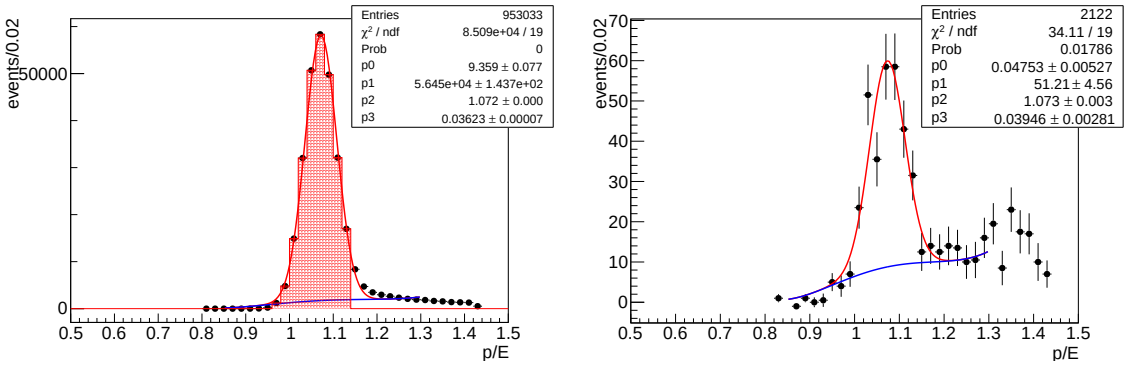

(a) MC (b) data

FIG. 14: p/E distributions in FCAL for the J/ψ peak fitted in the same way as for BH, data and MC

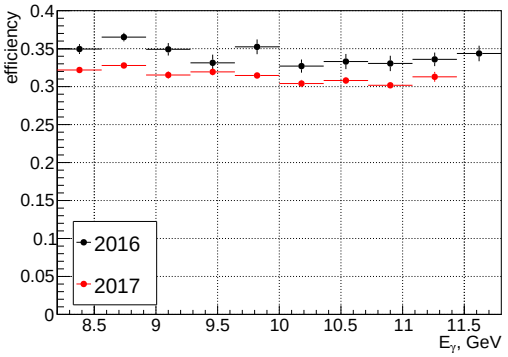

(a) BH($1.2 < M(e^+e^-) < 2.5$ GeV) efficiency as function of beam energy. Note: the low efficiency small $-t$ region in Fig.15b is excluded by applying $p_p > 0.4$ GeV.

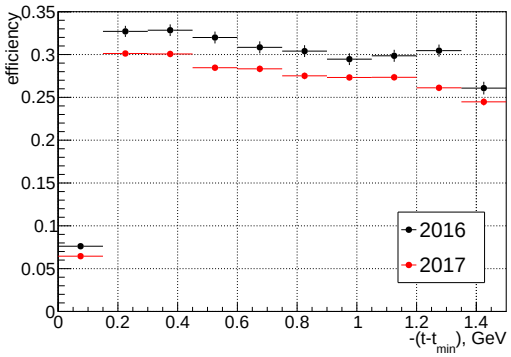

(b) BH($1.2 < M(e^+e^-) < 2.5$ GeV) efficiency vs $-(t - t_{min})$.

FIG. 15

is used for the reconstruction of the MC events. The efficiencies as function of E_γ and t are shown in Fig.15 separately for the 2016 and 2017 running conditions. The 2017 efficiency is consistently lower due to the higher rates, coming from higher background simulated by injecting "random hits" from the data. In both variables, E_γ and t, the efficiency doesn't vary significantly except at small t due to the proton having small momentum.

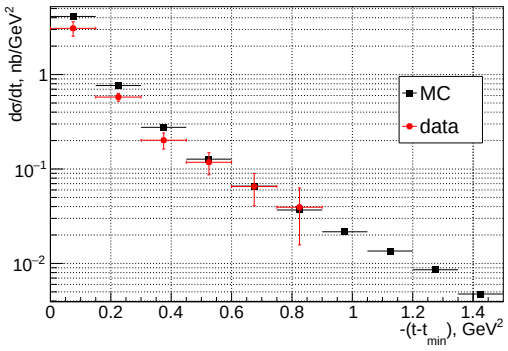

(a) The differential BH($1.2 < M(e^+e^-) < 2.5$ GeV) cross-section from the data compared to MC as function of $-(t - t_{min})$.

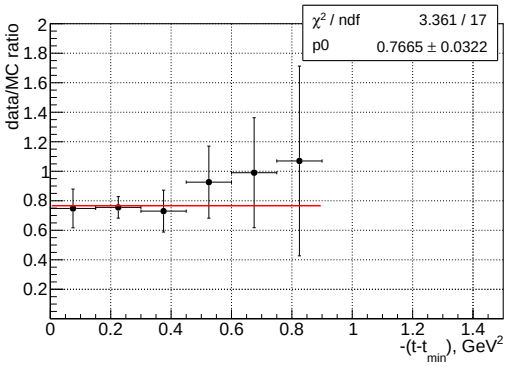

(b) Ratio of the data to MC (from Fig.16a) vs $-(t - t_{min})$ fitted with a constant.

FIG. 16

D. t-dependence

We start with the calculation of the BH cross-section as function of t. First, the BH yields are extracted using the fitting procedure described above (method (II)) in bins of $t - t_{min}$ using fixed signal widths. There's a significant increase in the background at high $-t$ values. For $-(t - t_{min}) > 0.9$ the electron/positron peak (like the one in Fig.12) is not visible and the spectrum is dominated by pions. This can be explained by a steeper t-dependence of the BH process w.r.t. to the pion background. The extracted electron/positron yields are corrected for the extra track combinations, which is a $\sim 5\%$ effect. Next we divide the yields by the efficiency from Fig.15b and the total flux to get the t-differential cross-section. Fig.16a compares the MC cross-section to the data and their ratio is shown in Fig.16b. The ratio is constant up to ~ 0.6 GeV^2 and then it increases. We conclude that this is an effect of the pion contamination and that there is no evidence for some systematic variation of the efficiency with t. Fitting the points up to 0.6 GeV^2 with a constant gives a value of 0.759 ± 0.056 that will be used as a COMMON normalization factor for the J/ψ $d\sigma/dt$ cross-section. This number also means that on average we have an additional (not taken into account by the simulations) inefficiency of about 24%.

Due to the increased π contamination we decided to use only the $-(t - t_{min}) <$ 0.6 GeV^2 region when using BH for normalization as function of beam energy. The effect of this cut is illustrated in Fig.17 showing the invariant mass spectra with and

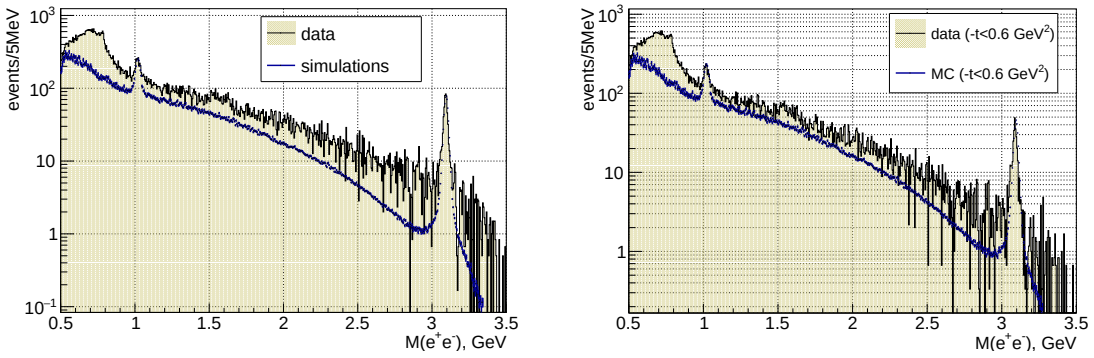

(a) Invariant mass spectrum compared to MC; no t-cuts are applied.

(b) Invariant mass spectrum compared to MC for $-(t - t_{min}) < 0.6$ GeV^2.

FIG. 17

without the t-cut – the MC and data are more consistent once the high t-values are cut out.

E. Beam energy dependence

Similar to the t-dependence, we extract the pion background and the BH signal in bins of E_γ separately in the BCAL and FCAL as explained in Sec.III B using method (II) and using fixed widths of the electron peak. The individual fits are shown in Figs.18,19 (10 bins from 8.2 to 11.8 GeV). We calculate the BH cross-section by dividing the yields by the flux (Fig.20) and efficiency (Fig.15). In Fig.21 we compare the measured cross-sections to the MC one and their ratio is shown in Fig.22. There are variations with the energy that may come from the flux and/or the efficiency. The difference in the energy spectrum for the 2016 and 2017 data sets, for which we know there's a difference in the efficiency not described by MC, may cause the variations, especially at the high energy end. Nevertheless, the ratio is statistically consistent with a constant, as demonstrated by the fit. Again, on average we have additional inefficiency that is not captured by MC of about 26%.

The reconstruction of the BH cross-section in this subsection using the flux was done only for the purpose of comparison with the BH calculations as a cross-check of the results. As explained in the next section, when reconstructing the J/ψ cross-section only the relative J/ψ-BH yields and the relative efficiency enters in the calculations, while the flux cancels out.

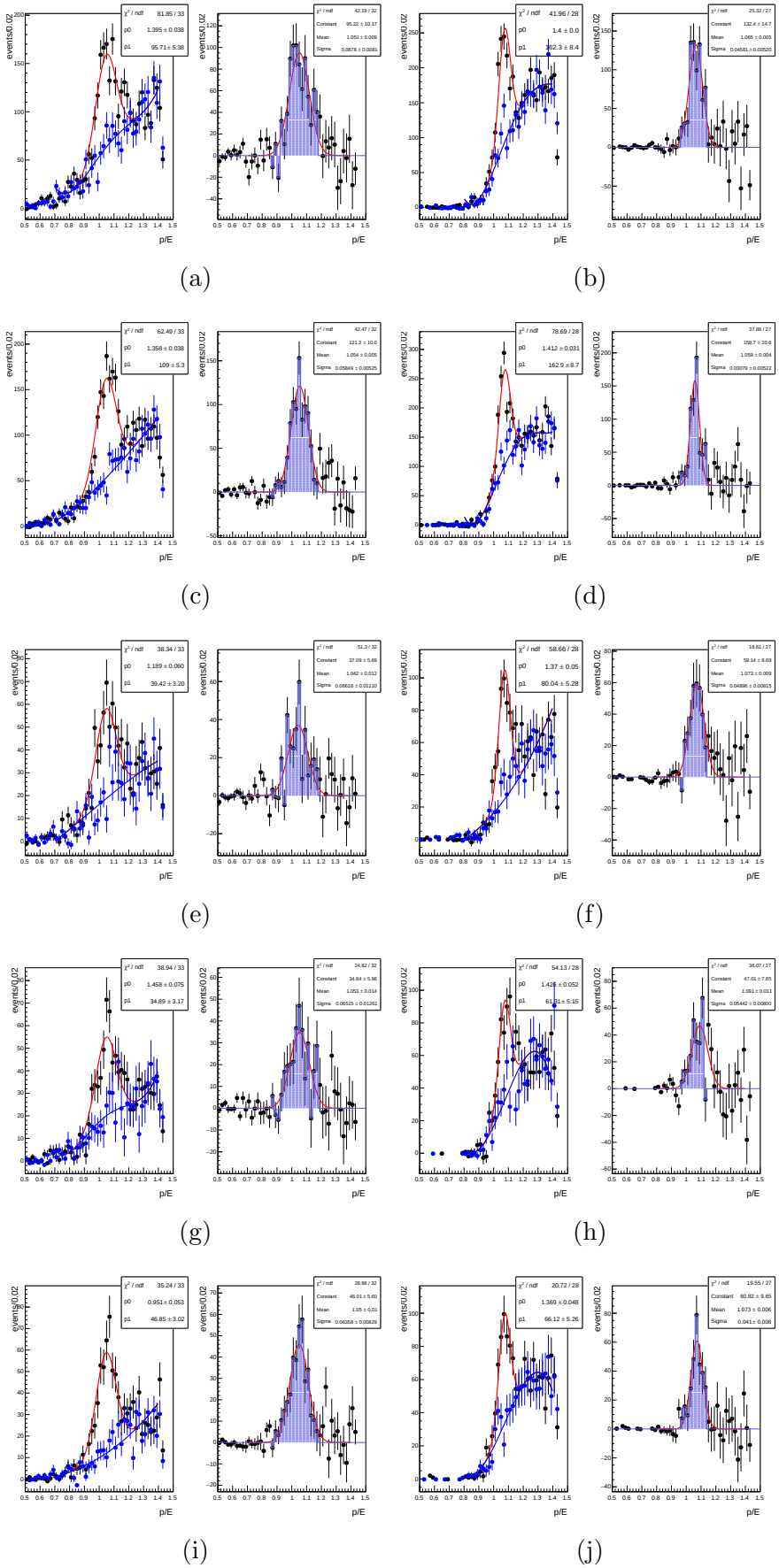

FIG. 18: Fits of p/E for BCAL(left pair of plots) and FCAL(right pair of plots) for energy bins 1-5. Left for the signal + pion background, right for the difference.

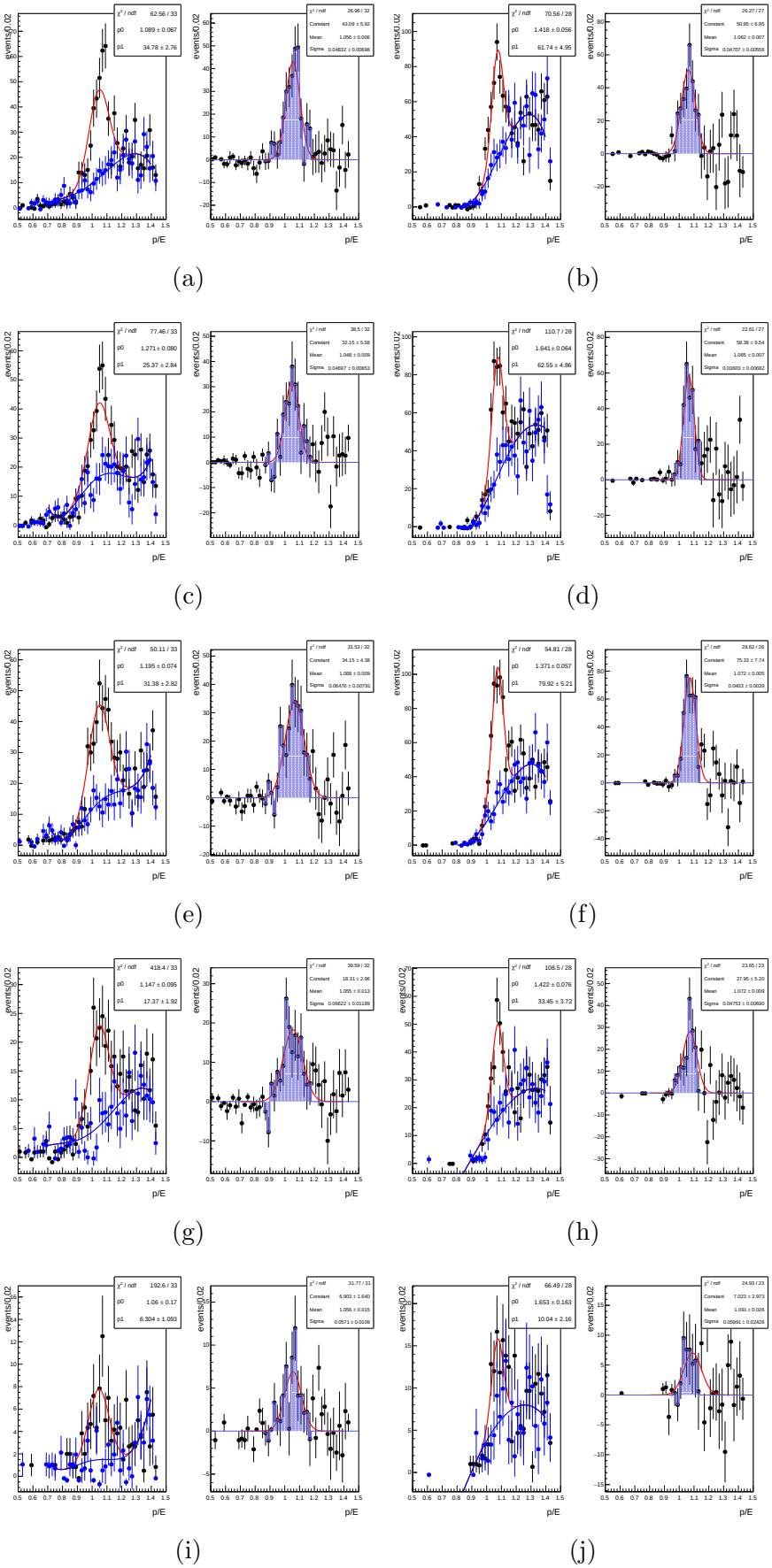

FIG. 19: Fits of p/E for BCAL(left pair of plots) and FCAL(right pair of plots) for energy bins 6-10. Left for the signal + pion background, right for the difference.

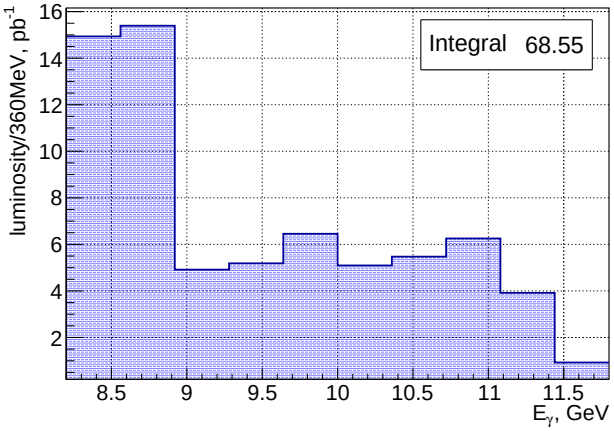

FIG. 20: Luminosity in bins of beam energy.

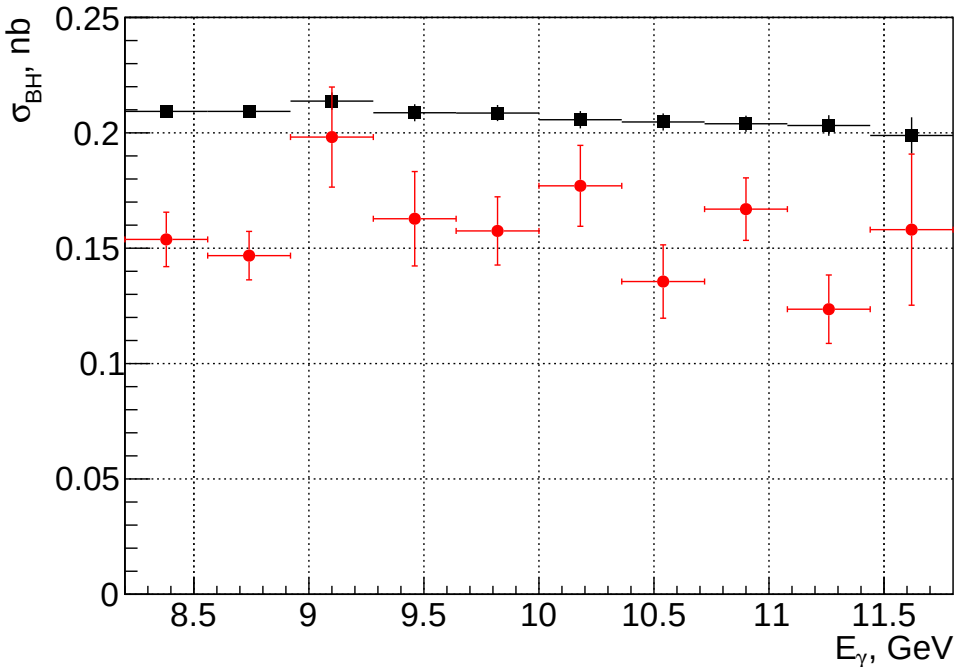

FIG. 21: BH($1.2 < M(e^+e^-) < 2.5$ GeV) cross-section extracted from the data (red) compared to MC (black) as a function of beam energy.

For the purpose of cross-checking and estimation of the systematics we have repeated the extraction of the BH yields for another two kinematic regions, as shown in Table IV. Also we have varied the fit procedure, using $2\sigma - 3\sigma$ range for the pion sample, and allowing variable peak widths. The corresponding results will be discussed in Section V.

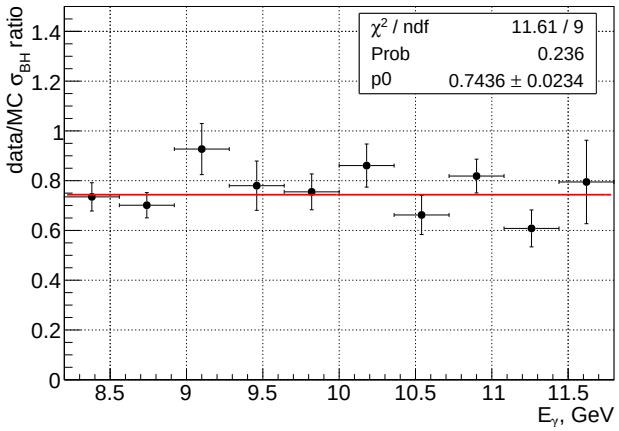

FIG. 22: Ratio of the data to MC cross-sections (from Fig.21) vs beam energy fitted with a constant.

setting	$M(e^+e^-)$ range, GeV	p_p range, GeV	$-(t-t_{min})$ range, GeV^2
(I) default	1.2-2.5	>0.4	0-0.6
(II)	1.5-2.5	>0.4	0-0.6
(III)	1.5-2.5	no limits	0-0.6

TABLE IV: Kinematic settings for BH used to check the systematics of the normalization.

variable	units	lower limit	upper limit
$-(t-t_{min})$ (for E_γ studies)	GeV^2	0	no limit
E_γ (for t studies)	GeV	10	11.8

TABLE V: Additional cuts applied for the J/ψ process.

IV. J/ψ PHOTOPRODUCTION

When studying the t-dependence of the J/ψ cross-section due to the limited statistics we have to integrate over some wide beam energy region. When the energy approaches the kinematical limit, $-t_{min}$ increases significantly and the t-range becomes narrower. Therefore, studying the t-dependence at the lower side of the spectrum requires slices in energy and much higher statistics. To be away from the threshold region we will investigate the t-dependence only for $E_\gamma > 10$ GeV, averaging ~ 11 GeV. As it will be clear in the next section, this region is very important to compare to the existing Cornell measurements [5] at 11 GeV and to be able to estimate the total cross-section from the SLAC data [6] at $E_\gamma > 13$ GeV. At the same time we are not restricting the t-range, as it was for the BH continuum, since the J/ψ mass peak is sitting on a very low background. The J/ψ cuts applied in addition to these defined in Section II, are shown in Table V.

A. Detector efficiency simulations

The J/ψ photoproduction is simulated using the *gen_jpsi* generator that is implemented within the standard *MCWrapper*. The procedure for the detector simulations is exactly the same as it was described in the previous section for the BH process.

The code generates the J/ψ-proton final state using an exponential t-dependence and a cross-section as a function of the beam energy. Then J/ψ decays assuming helicity conservation. For the final analysis we use a t-slope of 1.66 GeV^2, which is very close to slope extracted from the data, and an energy dependence from a fit of the extracted cross-section. These parameters have been varied in the simulations and, as discussed in Section V, the effect on the cross-section is relatively small.

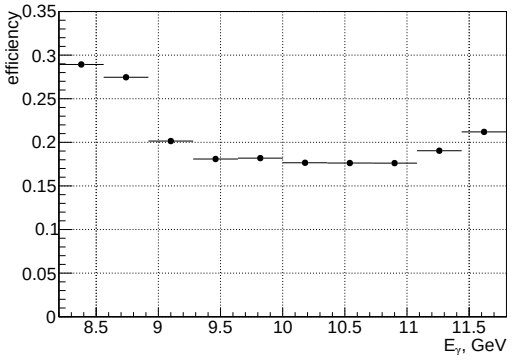

(a) J/ψ efficiency as function of beam energy.

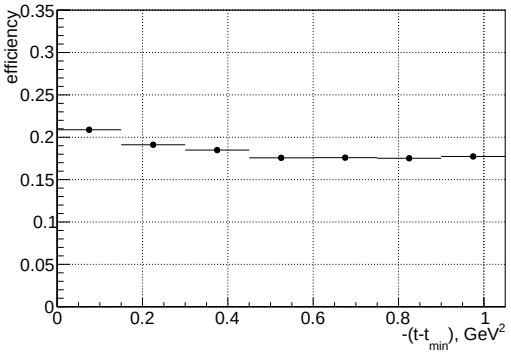

(b) J/ψ efficiency vs $-(t - t_{min})$.

FIG. 23

In Figs.23a and 23b we plot the efficiencies vs beam energy and t. These efficiencies, which will be used for cross-section calculations, have been obtained from fits of the MC distributions that include J/ψ signal and BH continuum, in bins of t and energy. We have used the same fit method that was used to fit the data, as described in the next subsection.

B. Peak fitting procedure

The invariant mass spectrum is accumulated separately for the in-time and out-of-time events. We have used several methods to fit these distribution and separate the signal from the background. These fits have been done in bins of energy and $(t - t_{min})$ as they will be used for cross-section calculations.

Here we will present only the method used in the final analysis as a result of extensive discussions with the review committee. The other methods that were studied can be found in the previous versions of the analysis paper.

We fit the invariant mass distributions **without subtracting the accidental background** with a linear background and a Gaussian. Thus, we will have in the histograms just number of events in which case we can use the likelihood method. As long as the accidental background is small and/or linear it will be effectively taken into account by the linear background component of the fitting function. To estimate the effect of the nonlinearity of the accidental distribution we use MC. In Fig.24 we compare the results of such fits with and without accidental subtractions. One can see that the yields are almost identical with

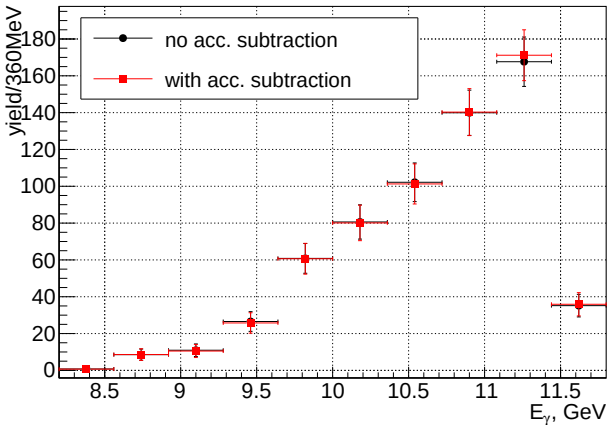

FIG. 24: Comparison of yields using likelihood fits with and without accidental subtraction in MC.

a maximum deviation of 2% which justifies the method. For the final results we use the binned likelihood method within the *RooFit* package where the yields are extracted from the fitted Gaussian. The corresponding fits in bins of $(t - t_{min})$ and energy are shown in Figs.25 and 26 respectively. In fact the results are almost identical if using *root* with the likelihood method.

Different variations of the fitting method will be discussed in Section V.

C. Cross-section: t-dependence

To calculate the differential cross-sections, the yields estimated from the fits in bins of $-(t - t_{min})$ are corrected for the extra track combinations ($\sim 6\%$ effect) then divided by the MC efficiency (Fig.23b) and the flux in the $10 - 11.8$ GeV beam energy region which is used for the t-dependence analysis. In addition we normalize the result by the J/ψ branching ratio and by an overall factor $C = 0.759 \pm 0.057$ from the BH normalization (Fig.16b):

$$d\sigma/dt = \frac{N_{J/\psi}(t)}{C\ \varepsilon_{J/\psi}(t) Flux(10-11.8 GeV) BR_{J/\psi} BW} \tag{3}$$

where BW is the t-bin width of 0.15 GeV. In Fig.27 we plot the differential cross-section extracted from the data. We obtain a t-slope of 1.665 ± 0.347 GeV^{-2}. We remind you that the beam energy interval used is $10 - 11.8$ GeV with an average of 10.72 GeV.

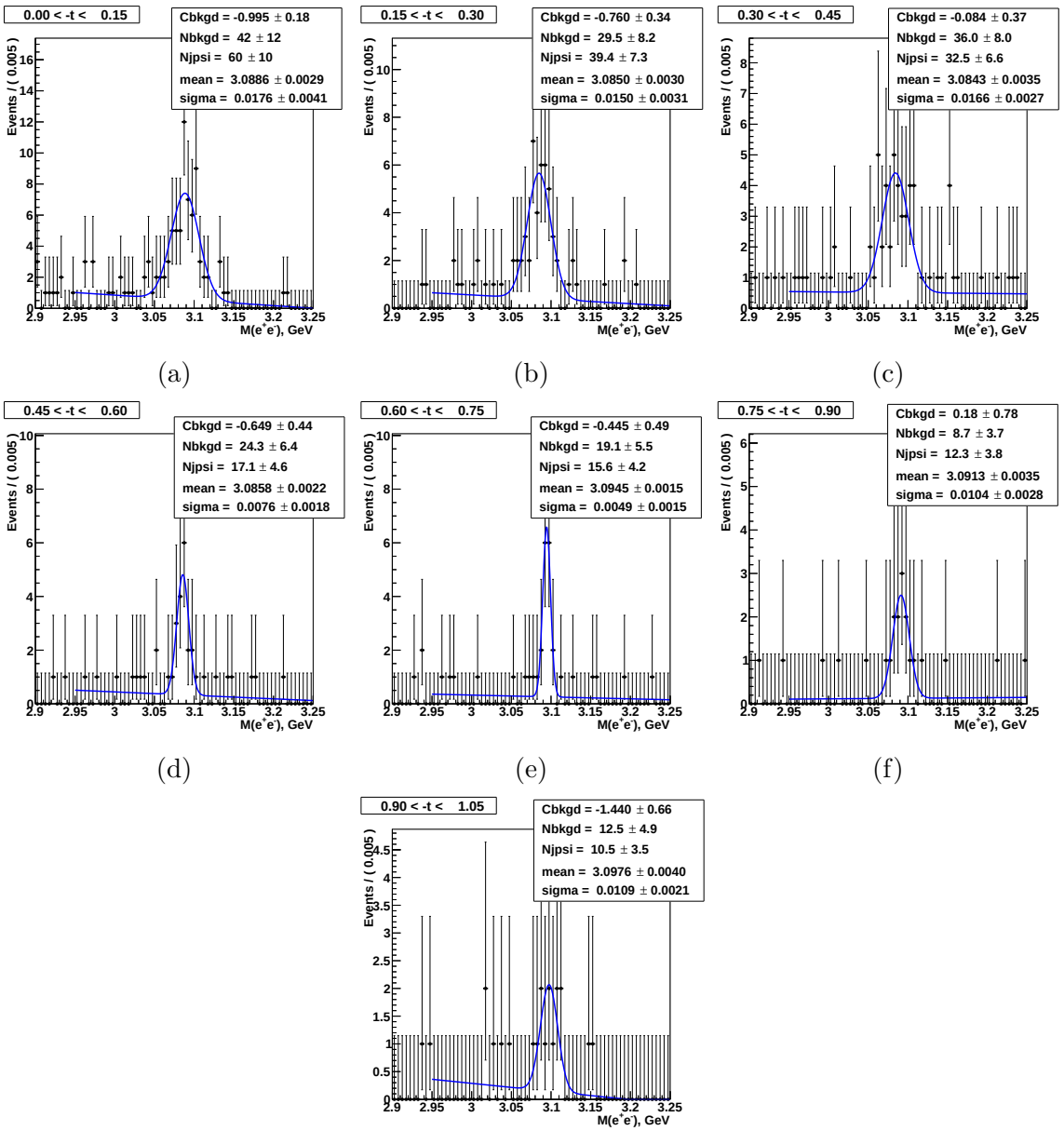

FIG. 25: Fits in bins of t.

D. Cross-section: beam energy dependence

We calculate the total cross-section as a function of energy using the following formulas:

$$\begin{aligned}\sigma(E) &= \frac{N_{J/\psi}(E)}{N_{BH}(E)}\ \frac{\sigma_{BH}(E)}{BR_{J/\psi}}\ \frac{\varepsilon_{BH}(E)}{\varepsilon_{J/\psi}(E)} \\ \sigma(E) &= \frac{N_{J/\psi}(E)}{N_{BH}(E)}\ \frac{N^{all}_{BH,MC}(E)}{flux_{MC}(E)}\ \frac{N^{cut}_{BH,MC}(E)}{N^{all}_{BH,MC}(E)}\ \frac{1}{BR_{J/\psi}\varepsilon_{J/\psi}(E)}\end{aligned} \tag{4}$$

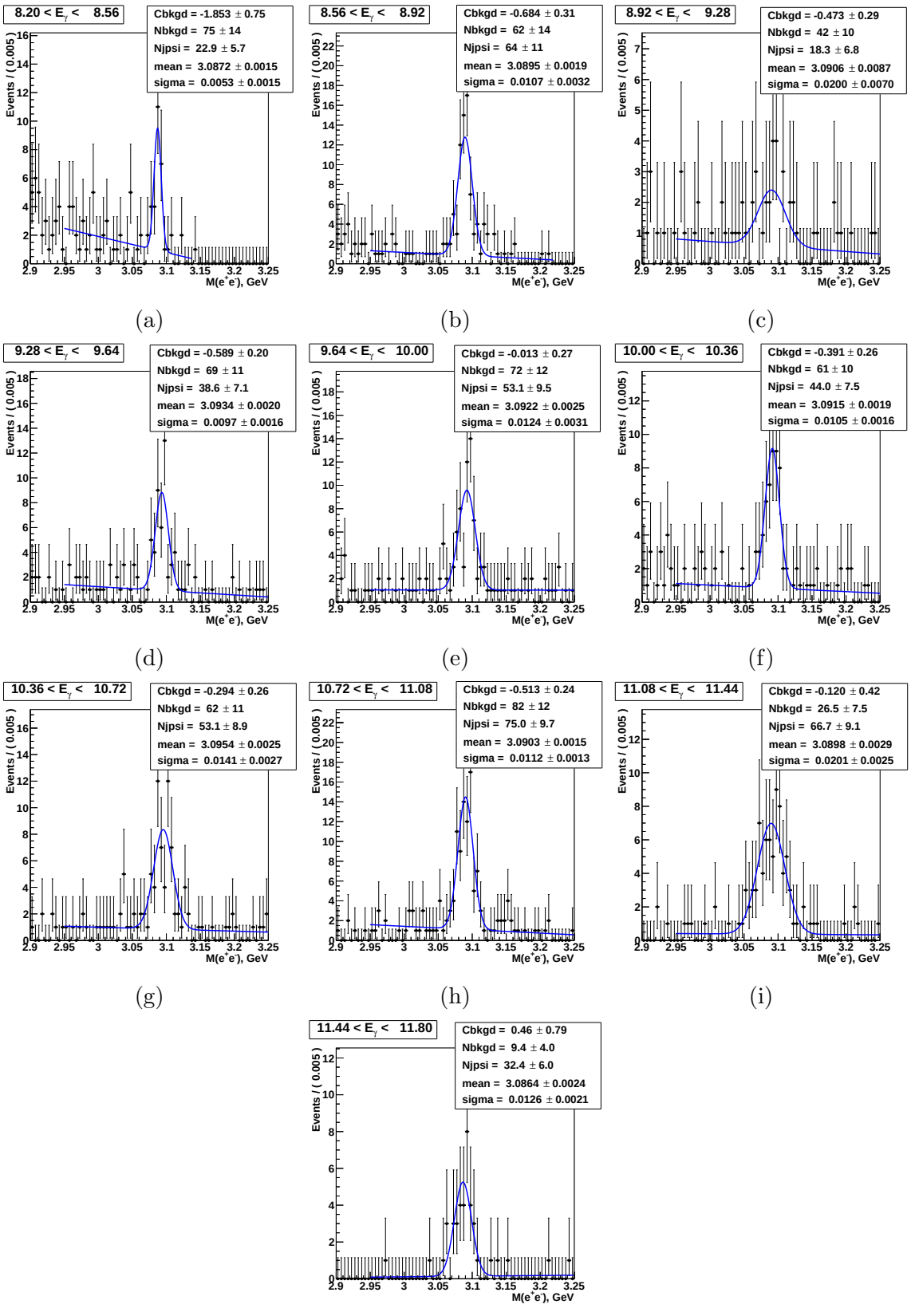

FIG. 26: Fits in bins of beam energy.

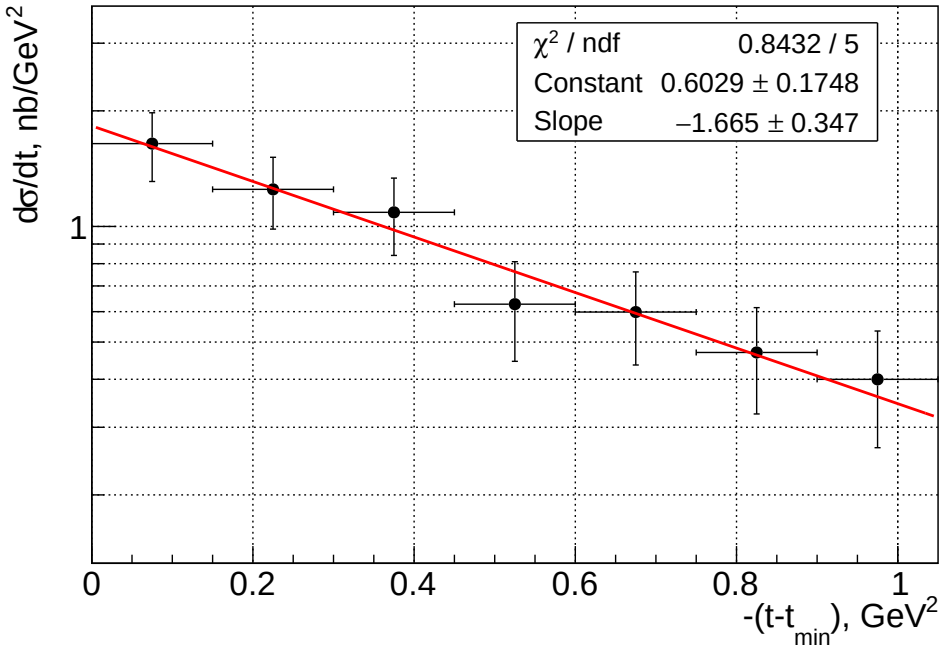

FIG. 27: Differential cross-section at $\langle E_\gamma \rangle = 10.72$ GeV vs $-(t - t_{min})$ fitted with an exponent.

Here $N_{J/\psi}$ and N_{BH} are the corresponding yields, σ_{BH} – BH cross-section, $BR_{J/\psi}$ – $J/\psi \to e^+e^-$ branching ratio, $\varepsilon_{J/\psi}$ and ε_{BH} – the efficiencies. The second line expands the BH cross-section as obtained from the thrown MC yield summed over a certain kinematic region and normalized by the MC flux. There also the BH efficiency is presented as a ratio of the final MC yields (after applying the same cut as for the N_{BH} yield) to the thrown yields. One can see that in the final result the thrown MC yield cancels out which means that it doesn't matter which kinematic region is used for normalization, important are only the MC yields after applying all the cuts used for the data.

In Fig.28 we demonstrate the effects of the different terms in Eq.4. Shown is the ratio of the yields multiplied by $\sigma_{BH}(E)/BR_{J/\psi}$, where the Bethe-Heitler cross-section is well under control, being almost constant with the energy (Fig.21) for the $1.2 - 2.5$ GeV invariant mass range. The most important correction (up to a factor of 1.75) comes from the ratio of the efficiencies – black to red data points on the plot.

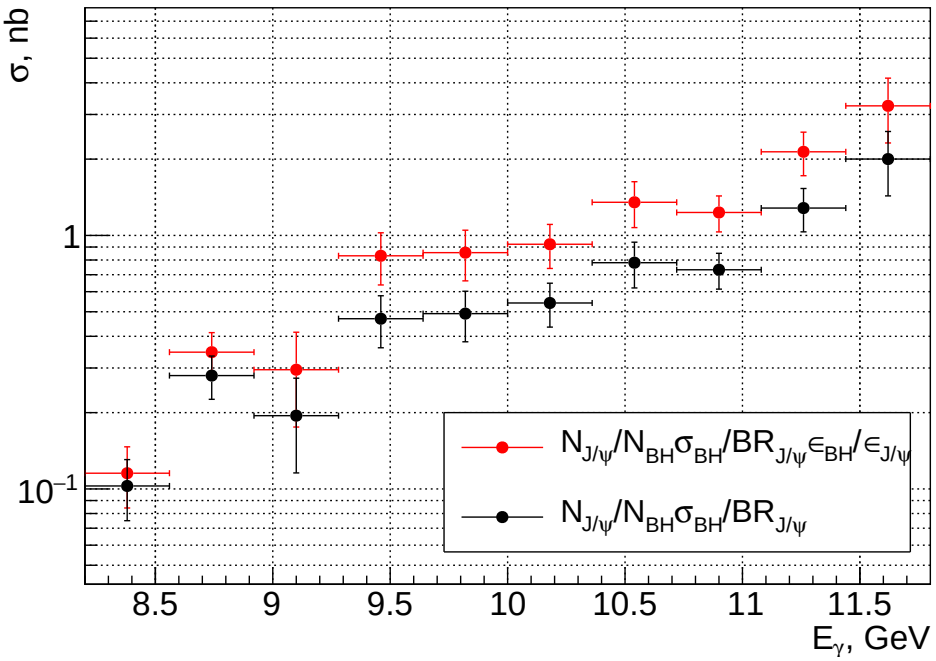

FIG. 28: Different factors in the calculations of total cross-section vs beam energy.

V. SYSTEMATICS

Some of the sources of systematic uncertainties were discussed in the previous subsections in relation to the corresponding analysis. The purpose of this section is to discuss all the related analysis and have a complete list of the systematic errors in one place.

A. 2016 vs 2017 data set

We know that when comparing the results from the 2016 and 2017 data sets we see discrepancies in the flux-normalized yields of about $20-40\%$ which are well established for the high cross-section channels but not yet understood. After introducing data-driven random hits, about 10% of the effect was explained by MC due to the difference in the intensities for the two running periods. At the same time in 2017 there was a drastic change of the beam intensity. Still the agreement between the low- and high-intensity periods in that year is much better than both periods compared to the 2016 data. Thus, we are dealing with an unknown source of uncertainty that we have to take into account.

Figs.29a,29b demonstrate the 2016/2017 discrepancy for the BH process. Due to low

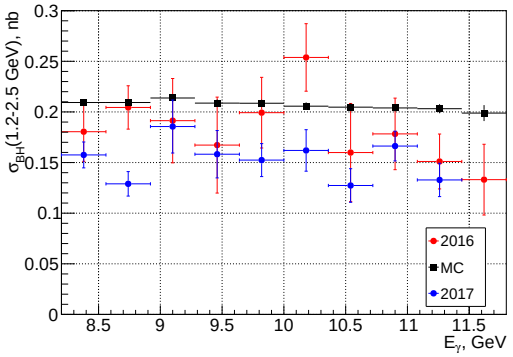

(a) BH cross-section as function of beam energy for MC and the two running periods.

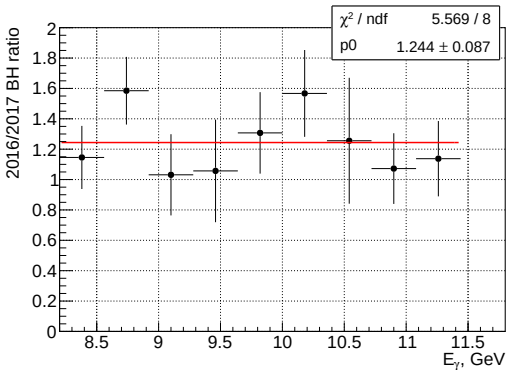

(b) 2016/2017 ratio of the points from Fig.29a.

FIG. 29

statistics these results are not so conclusive as in the case of high cross-section reactions. We see that both sets of data require an additional inefficiency in the BH simulations, at the same time their ratio (Fig.29b) shows the 2016 BH cross-section is higher by $\sim 24 \pm 9\%$.

Similarly, for the J/ψ cross-section without BH normalization we see (Figs.30a,30b) the 2016/2017 ratio is 1.26 ± 0.16. The important question is however, if we normalize to BH, does the J/ψ cross-section changes between 2016 and 2017. From Figs.31a,31b we see that in this case the 2016/2017 ratio is consistent with unity: 0.95 ± 0.14. Therefore, whatever the source of the discrepancy between the 2016 and 2017 data sets is, it cancels (within the statistical errors) when using BH for normalization and we don't see a reason to add a contribution to the systematical error related to this source.

B. BH J/ψ relative efficiency

Since we are using BH for normalization, the result for the cross-section depends on the relative BH-J/ψ efficiency which is the most significant source of systematic uncertainties. In Fig.32 we compare the two efficiencies as function of E_γ. To better understand the relative efficiency we compare in Fig.33 the 2D efficiencies vs proton momentum and polar angle. The topographic lines represent the beam energy. In case of BH they are shown at $M(e^+e^-) = 1.5$ GeV and will move to the left-upper corner as the invariant mass increases and approaches the J/ψ mass. One can see that during such a move the efficiency varies up

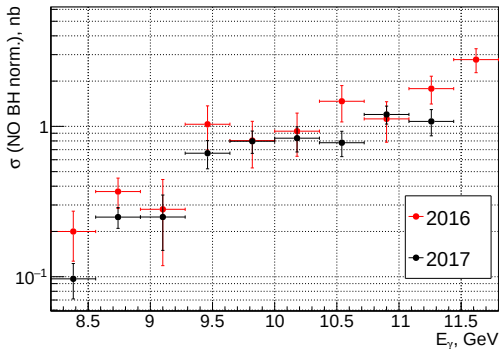

(a) J/ψ cross-sections vs energy for the two running periods without BH normalization.

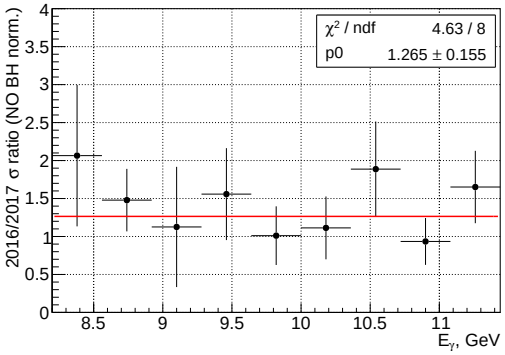

(b) 2016/2017 cross-section ratio from Fig.30a without BH normalization.

FIG. 30

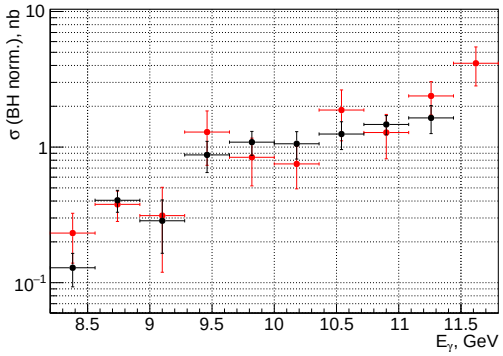

(a) J/ψ cross-sections vs energy for the two running periods normalized with BH.

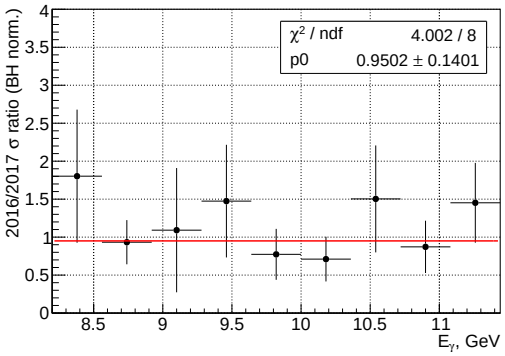

(b) 2016/2017 cross-section ratio from Fig.31a normalized with BH.

FIG. 31

to a factor of 2, noticeably when passing the CDC-FDC transition region.

When the energy approaches the J/ψ threshold, the $-t_{min}$ value and therefore the proton momentum increases. At the same time the protons are directed more forward and away from the CDC-FDC transition region. All of this results in a higher J/ψ efficiency at small E_γ as can be seen from Fig.33a. The BH efficiency drops at small $(t - t_{min})$ due to the small proton momentum, which is not the case for J/ψ production. Note that for the BH efficiency vs E_γ small t-values are excluded by the cut $p_p > 0.4$ GeV.

In order to verify these effects experimentally the CDC-FDC transition region was studied with a controlled pion sample (using $\omega \to 3\pi$ events with one missing pion) and good agreement (so far) was found between data and MC [7]. However, in these studies, we

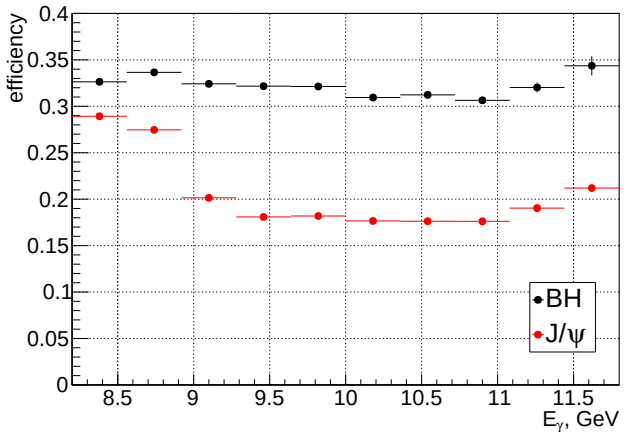

FIG. 32: J/ψ vs BH efficiency as function of beam energy.

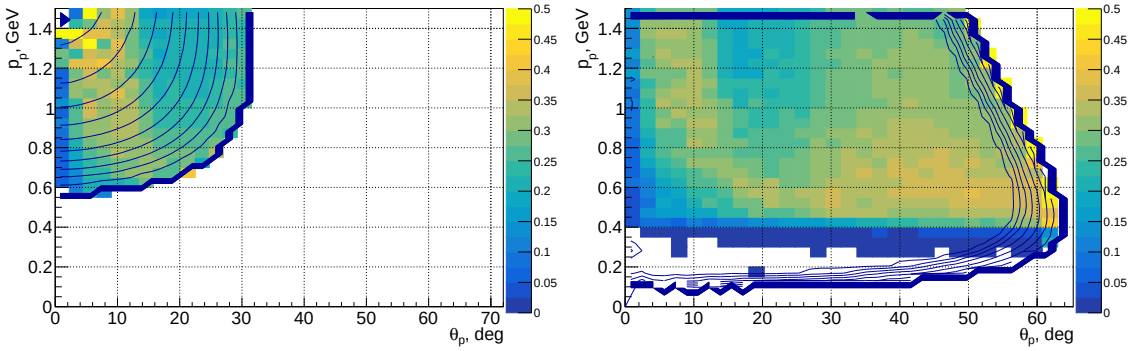

(a) J/ψ (b) BH

FIG. 33: Efficiency vs proton momentum and polar angle for J/ψ and BH. The topographic lines correspond to different beam energies increasing from left to right. In case of BH they refer to $M(e^+e^-) = 1.5$ GeV.

don't observe such a drop of the efficiency. While the reason for the proton inefficiency in this region is unclear one hypothesis is that the protons lose energy in the CDC end-plate producing secondaries that distort the tracking. Reaching this region with protons can be done only for high invariant masses. We will use again the BH process to verify the efficiencies. An attempt has been made to scan the BH invariant mass spectrum up to the J/ψ peak (see next subsection) however it turned out that above 2.5 GeV the cross-section is below the sensitivity of these measurements. Instead, we show here results of comparing the data and MC for the BH process below 2.5 GeV as function of the proton angle (Figs.35,36) and momentum (Fig.34). The important regions in these plots are $\theta_p < 30^0$ and $p_p > 0.6$ GeV, corresponding to the J/ψ kinematics, though with BH they are not covered

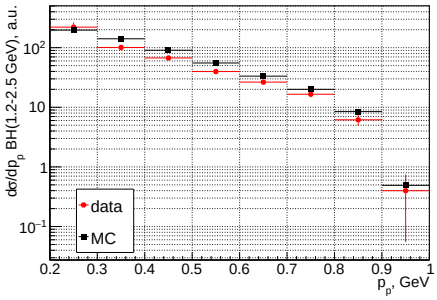

(a) Data vs MC BH cross-section as function of the proton momentum.

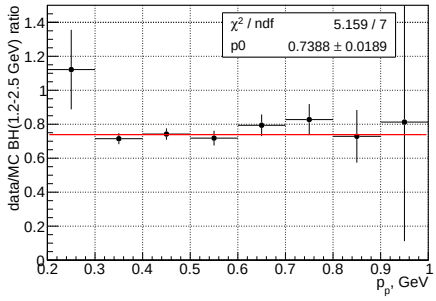

(b) Data/MC ratio for BH cross-section (for $1.2 < M(e^+, e^-) < 2.5$ GeV) as function of the proton momentum.

FIG. 34

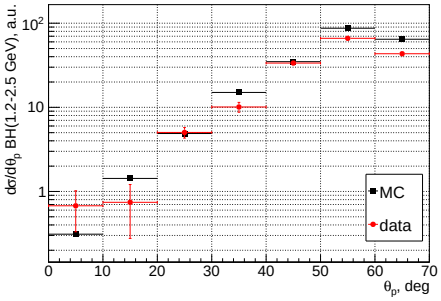

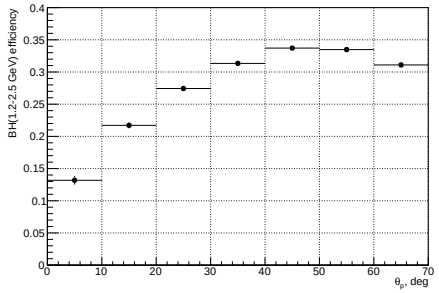

FIG. 35: Data vs MC BH cross-section (left) and efficiency (right) as function of the proton angle.

at the same time. We see that there are no significant variations of the data/MC ratio with p_p (though for big proton angles) despite the significant variations in the cross-section. As for the θ_p dependence, we see a deviation of the data/MC ratio in the $10 < \theta_p < 30^0$ region (dominated by small proton momenta) of $23\% \pm 17.7\%$ which is not statistically significant,

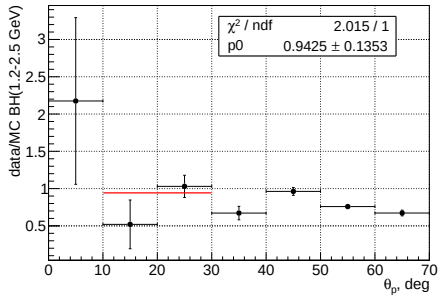

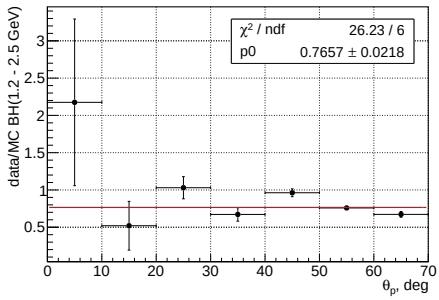

FIG. 36: Data/MC ratio for BH cross-section (for $1.2 < M(e^+, e^-) < 2.5$ GeV) as function of the proton angle for two different fitting ranges.

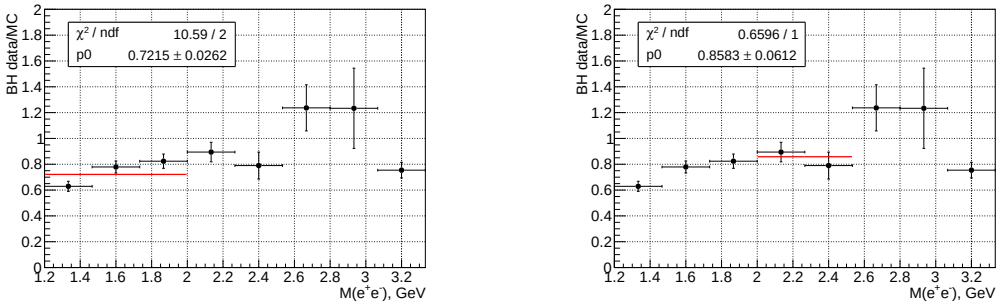

FIG. 37: Data/MC ratio for BH cross-section as function of the invariant mass, fitted in two ranges that includes/excludes the position of the $\rho'(1600)$ resonance.

event the cross-section and efficiency ((Figs.35) vary significantly. Based on this, we will assume 23% systematic error for the relative J/ψ-BH efficiency.

C. ρ' contribution

To estimate the effect of the possible $\rho'(1600)$ production we plot (Fig.37) the ratio of the data to MC for the BH cross-section as function of the invariant mass. Fitting the ratio in the two regions, $1.2-2$ and $2-2.5$ GeV, gives us an estimate for the upper limit of possible ρ' contribution of 7%.

D. Radiative effects

The external radiation of the electrons is included in the simulations. It results in a tail in the the J/ψ invariant mass when reconstructed from the measured quantities of the two leptons. If using the missing mass off the proton, there are no radiative effects and no tail in the invariant mass. Similarly, if using the kinematic fit quantities, the tail almost completely disappears – Fig.38. This is explained by the fact that it is the proton that mostly constrains the fit.

The effect of the internal radiation that occurs at reaction level may be different for the J/ψ photoproduction and the BH process. In case of the J/ψ production, the radiation of the electron-positron pair from the J/ψ decay is decoupled from the proton that is involved only in the production of the J/ψ. This is not the case for the BH process where the electron-positron pair and the recoil proton are part of the same reaction.

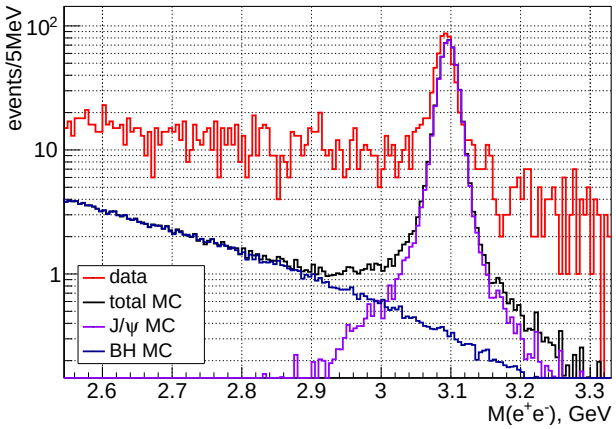

FIG. 38: Data (including pion contamination) vs MC that includes BH and J/ψ in the high invariant mass region.

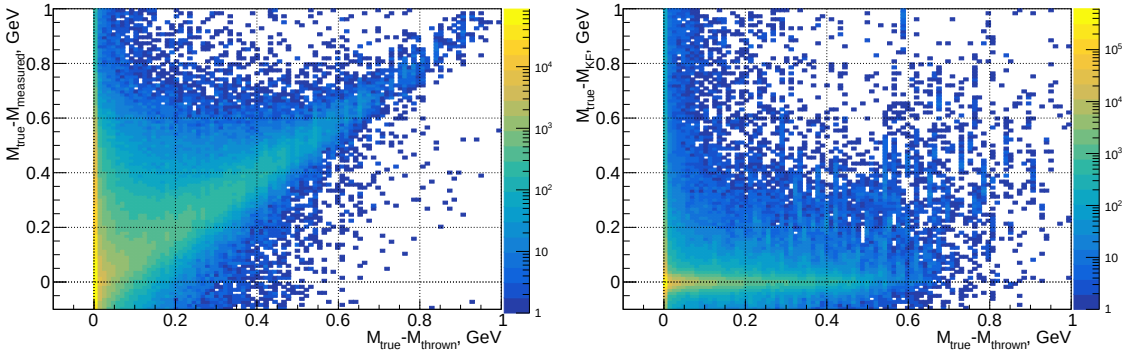

(a) Using measured invariant mass.

(b) Using kinematic fit.

FIG. 39: J/ψ simulations using PHOTOS [8]. X-axis: difference between the true J/ψ mass and the thrown one after radiation. Y-axis: difference between the true mass and the reconstructed one when using measured quantities (a) or the kinematic fit (b).

The internal radiation was included into the simulation of the J/ψ decay using the PHOTOS code [8]. The results are illustrated in Fig.39 showing the effect of the radiation on the reconstructed invariant mass when using measured quantities or the kinematic fit. The measured invariant mass shows clear correlation with the radiation (Fig.39a) while the kinematic fit restores the invariant mass before the radiation. As a result we don't observe any difference in the efficiency with and without radiation.

In [9] the radiative corrections (RC) for the BH process are calculated in the soft photon approximation. The radiative correction $\delta_{RC}(\Delta E)$ defined as:

$$\sigma_{BH,R} = \sigma_{BH}\left[1 - \delta_{RC}(\Delta E)\right] \tag{5}$$

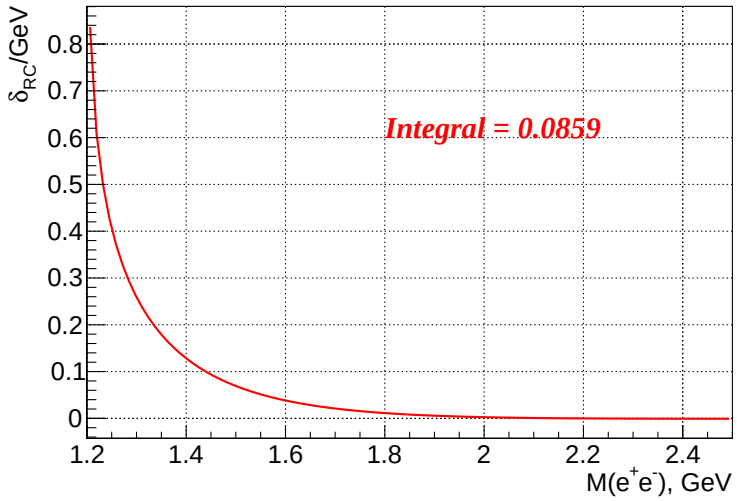

FIG. 40: RC (Eq.6) to the BH cross-section per 1 GeV invariant mass (Eq.6). The integral gives the total "leakage" (through the lower BH limit) of 8.6%.

are given by Eq.(65) in that paper, where $\sigma_{BH,R}$ is the observed BH cross-section that corresponds to a certain cut of the photon energy ΔE, given in the c.m. of the electron, positron, and photon. When using the missing mass off the recoil proton, M_{miss}, we obtain from Eq.(57) for soft photons that $\Delta E = M_{miss} - M(e^+, e^-)$, where $M(e^+, e^-)$ is the e^+e^- invariant mass after the radiation. The maximum change of M_{miss} corresponds to the case when the two leptons remain intact, i.e. $M(e^+, e^-)$ is equal to the true invariant mass before radiation, M_{true}, and the radiation affects only the proton, in which case we have $\Delta E = M_{miss} - M_{true}$.

We parametrize the true BH $d\sigma/dM$ cross-section as $e^{-2.8M_{true}}$ and normalize it to its integral (Int) within the invariant mass limits, M_{low} and M_{high}. To estimate the leakage through the lower limit, we fold it with $\delta_{RC}(\Delta E)$ from Eq.(65):

$$\delta_{RC}(M) = \frac{e^{-2.8M_{true}}}{Int}\frac{\alpha}{\pi}\left\{ln\frac{4(M_{low}-M_{true})^2}{M_{true}^2}\left[1+ln\frac{m_e^2}{M_{true}^2}\right]-\frac{\pi^2}{3}\right\} \quad (6)$$

where we have replaced $\Delta E = M_{low} - M_{true}$ and $s_{ll} = M_{true}$. The integral of Eq.6 (see Fig.40) is an estimate of the total effect of 8.6%. Similarly, we estimate the leakage thought the upper limit into the invariant mass interval to be of 0.3%, resulting in 8.3% RC to the BH cross-section. This is an estimation of the upper limit on the radiative correction when using the missing mass off the proton.

Studying the BH radiative corrections in case of the kinematic fit requires MC simulation of the $\gamma p \to e^+e^-\gamma_{soft}p$ process, using some model for modification of the energies and angles of the final state particles due to the photon emission. For this purpose we have used PHOTOS [8] to simulate the "decay" of the e^+e^-p system producing soft photons. We found that when using the kinematic fit the efficiency is the same with and without radiation within the statistical error of a percent.

In summary, the maximum correction to the BH cross-section corresponds to the case when the proton takes all the effect of the soft photon radiation, that we estimated to be 8.3%. If true, it will lower the J/ψ cross-section by that percentage.

E. Timelike Compton Scattering

In addition to the electromagnetic processes, the Timelike Compton Scattering (TCS) may contribute to the e^+e^- continuum. We use 8% uncertainty as a conservative limit of the possible TCS contribution [10].

F. Exclusiveness of the reaction

In Fig.41 we compare the missing mass squared distribution from data and MC for $M(e^+e^-) > 1.2$ GeV. The MC distribution is fitted with a three-parameter function, $p1/(p2+x)^{p3}$, separately for positive and negative x-values. Then, the data distribution is fitted with the same shape times a normalization coefficient. One can see that at both sides, negative and positive, the data show wider distribution. No peak around pion mass squared (0.0195 GeV^2) is visible.

To have an upper limit of a possible pion contribution we assume that the enhancement above MC shape at the right shoulder is coming only from pions. We fit the data (Fig.42) with the MC shape plus a Gaussian, representing the pion contribution, centered at the pion mass with a variable amplitude (p1) and width (p3). Integrating the areas below the pion peak and the total distribution we obtain a maximum possible contribution from pions of 5.0%.

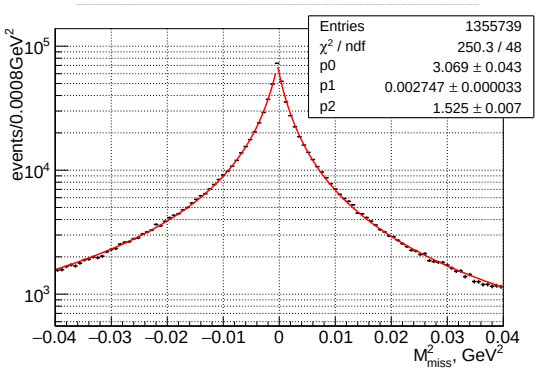

(a) Missing mass squared distribution for $M(e^+e^-) > 1.2$ GeV for MC fitted with $p0/(x+p1)^{p3}$ separately for the positive and negative x-values.

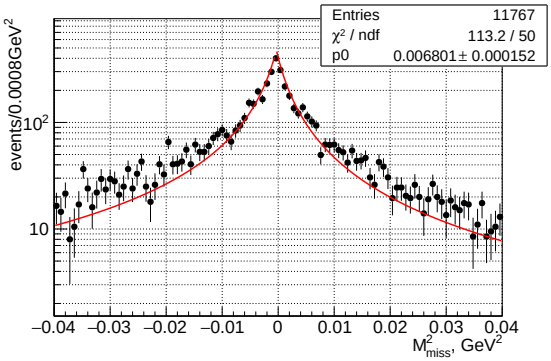

(b) Missing mass squared distribution for $M(e^+e^-) > 1.2$ GeV for data fitted with the same functional shape as for MC times one normalization coefficient.

FIG. 41

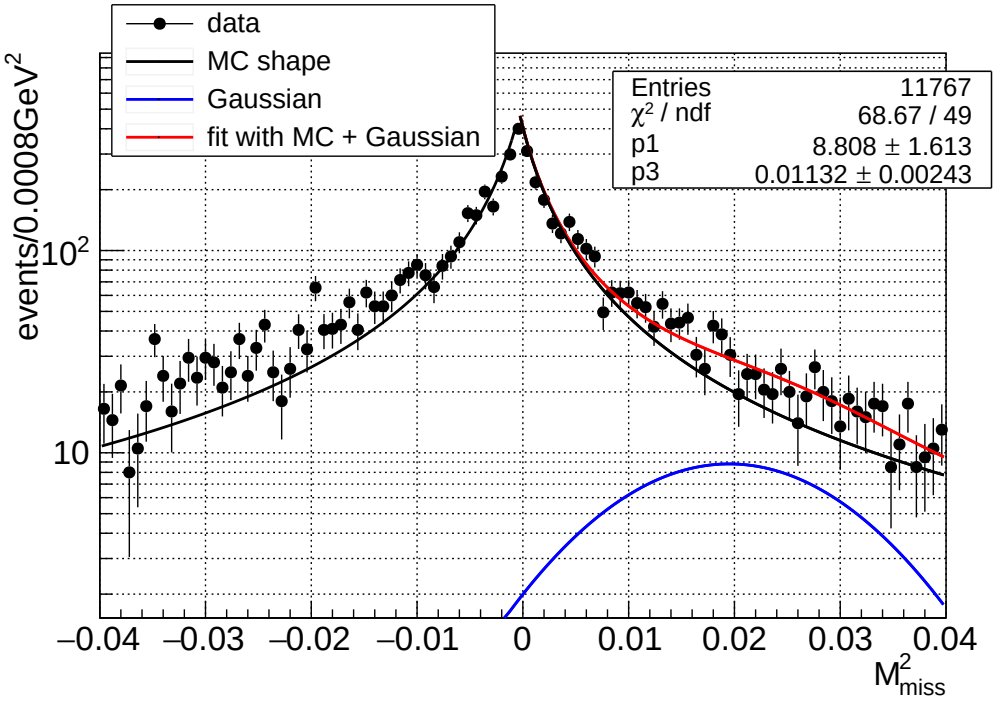

FIG. 42: Data points (same as in Fig.41b) fitted (red) with MC shape (black) plus Gaussian (blue) giving an upper limit of a possible pion contribution to the total of 5.0% – see text.

G. Point-to-point systematics

We will discuss first the point-to-point (p.t.p.) systematical errors for the total cross-section in bins of beam energy. The results for the differential cross-section in bins of t

obtained in the same way as for the E_γ dependence, will be shown at the end of the section. We define the p.t.p. systematics as an R.M.S. of the results obtained when varying certain parameter or procedure. To total p.t.p. systematics is a quadratic sum of the errors coming from the different sources.

1. Systematics in the J/ψ yield fitting

We use different methods of fitting the J/ψ peak to estimate the systematics of this procedure. It was discussed whether one can fix some of the parameters (mean and width of the peak) based on the fit of the total distributions or MC. As seen from Fig.26 the widths of the third and ninth bins are ~ 20 MeV, the first bin is 5.3 MeV, while the rest are between $10-13$ MeV. This can be explained partially by the mixture of the 2016 and 2017 data sets with different solenoid fields, energy end-points and position of the coherent peak. Moreover, between production versions 2 and 3 the resolutions drastically changed, on average from 7.5 to 13MeV. All these features are not reproduced in MC, showing resolutions between 9 and 14 MeV indicating hidden effects not taken into account by MC. Therefore, fixing the widths will introduce a systematic error.

Alternatively, we can use the fits only to estimate the background. Then we subtract the background and in the resulting histogram we count the number of events within 3σ of the mean, where the σ and the mean values are obtained from the fit of the total distribution and are fixed for all the bins.

In Fig.43 we compare the results of the different methods: varying vs fixing the width and integrating vs counting the events. One can see that indeed, fixing the width in the fit and integrating results in big (up to 25 %) deviations deviations from the rest. At the same time, there's a good agreement between integrating and counting when σ is variable with a maximum deviation of 6% for the fifth point, to be compared to the statistical error of 17% there.

The R.M.S. of these variations for each point is used to estimate the systematical error.

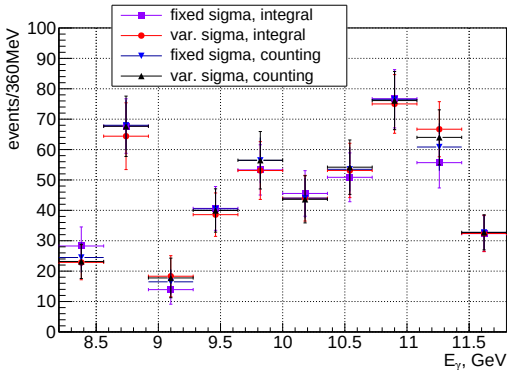

(a) Comparison of the yields obtained by integrating the fitted Gaussian or by counting the number of events within 3σ ($\sigma = 12.5$ MeV), with/without fixing σ in the fit.

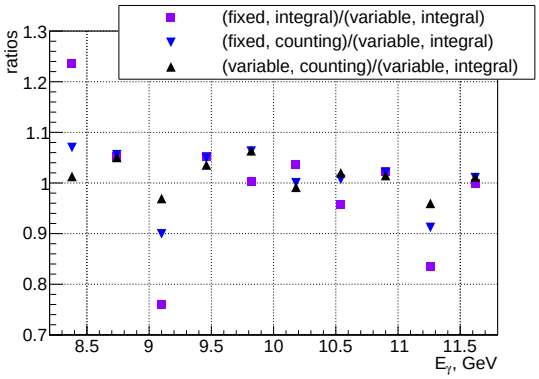

(b) Ratios of the yields, without error bars, from Fig.43a to the nominal method (integration and variable width).

FIG. 43

2. Systematics in the BH yield fitting

We vary the cut used to create the pion sample in two regions: $2-4\sigma$ (default) and $3-4\sigma$ from the electron peak. Another variation is fitting with a fixed σ (default) and having it as a free parameter. The effect of these different fits on the cross-section is shown in Fig.45.

We also study the effect of the different BH normalization ranges (Table IV) on the cross-section – Fig.46. If applying the $p_p > 0.4$ GeV cut the two invariant mass ranges give very similar results (red vs blue data points). Comparing the effect of the p_p cut (blue vs black) in most of the points we see some increase of the cross-section.

3. Varying J/ψ simulation parameters

Since the cross-section depends strongly on both, energy and t, it is important first to analyze the two-dimensional efficiency shown in Fig.47. The most important region is near t_{min} where the cross-section is maximal. When approaching t_{min} we see an increase in the efficiency and then a sharp decrease at the kinematic limit. There's a delicate balance in this region between two effects, an increase in the proton momentum which increases the efficiency and a decrease of the polar angle so that at the limit the proton is produced in the forward direction where there's no detection. It is obvious that assumptions about the

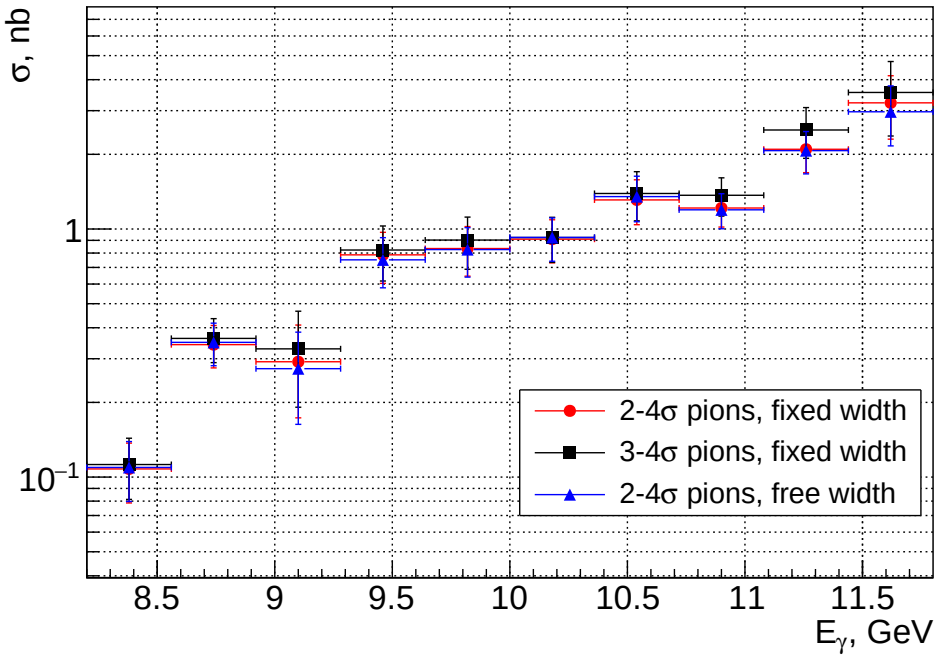

FIG. 44: Effect of the different BH fitting procedures on the total cross-section vs beam energy.

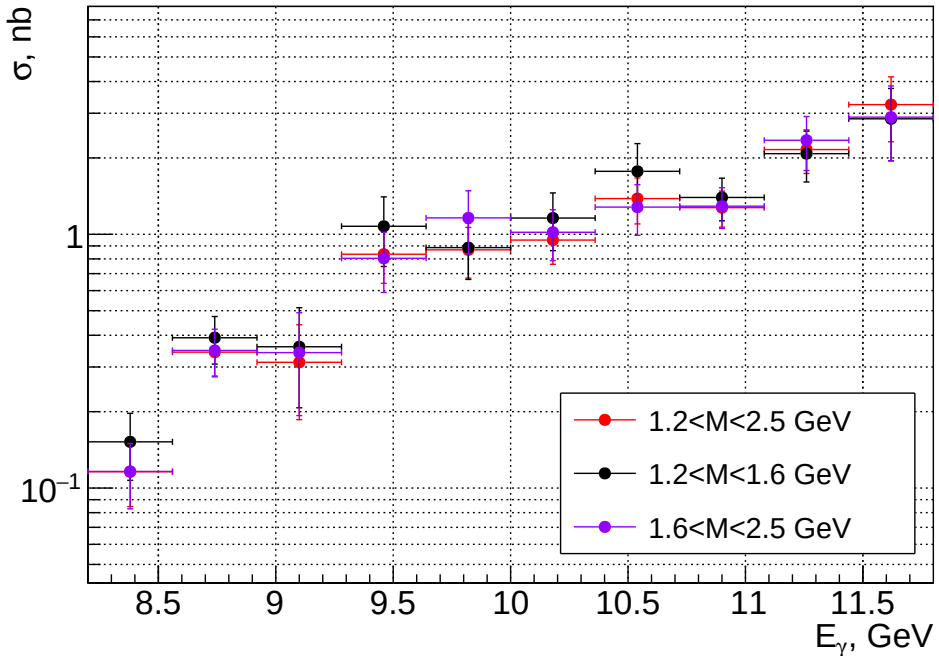

FIG. 45: Effect of the different BH fitting procedures on the total cross-section vs beam energy.

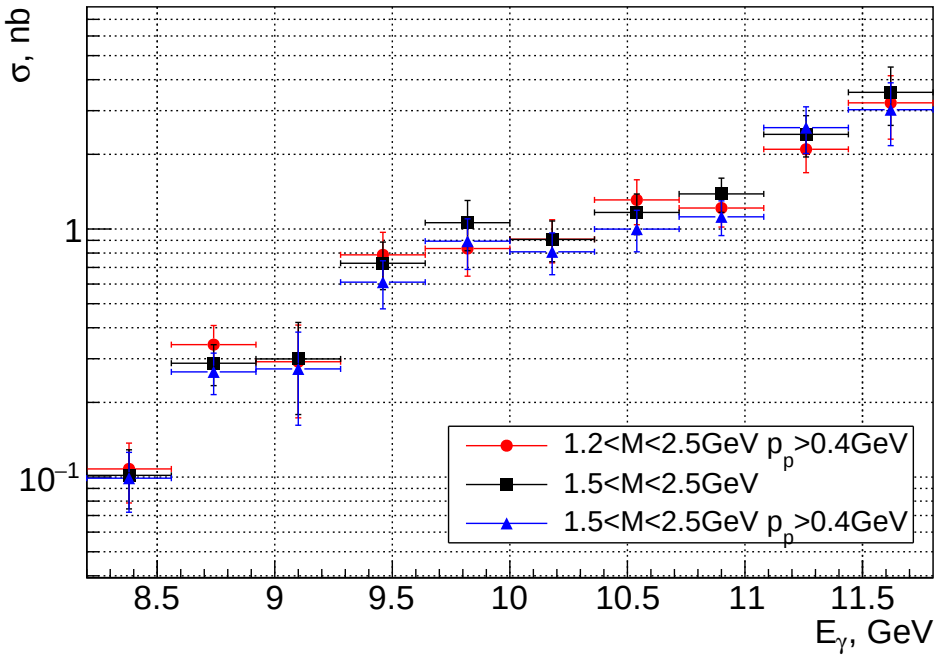

FIG. 46: Effect of the different BH normalizations on the total cross-section vs beam energy.

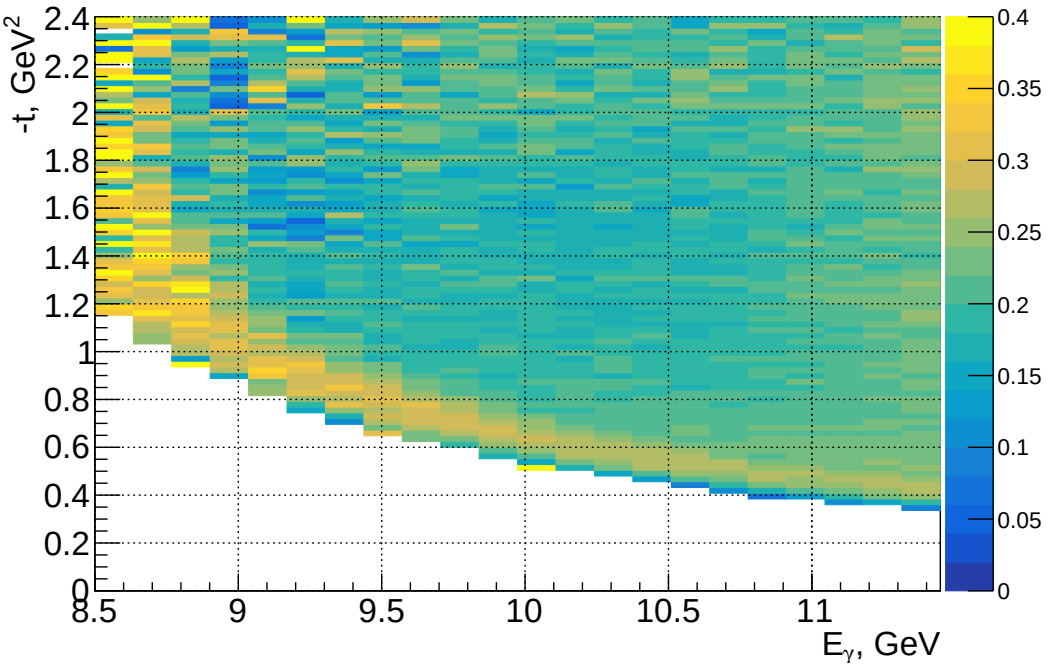

FIG. 47: J/ψ 2D-efficiency as function of beam energy and t.

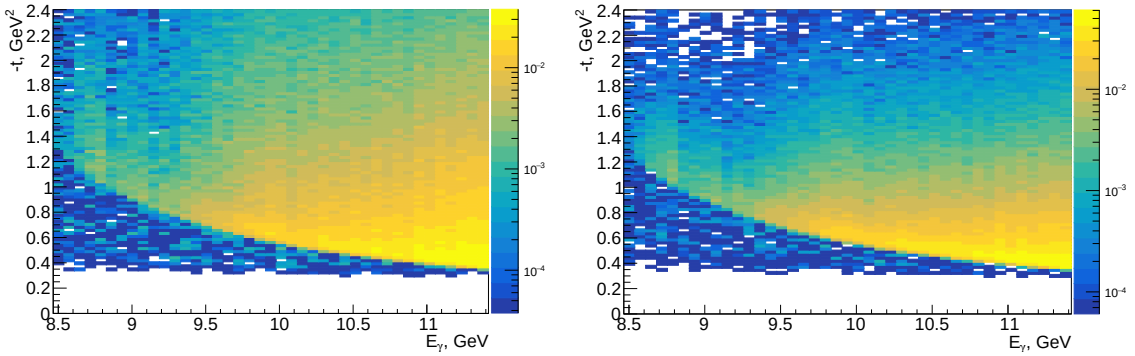

(a) J/ψ MC yields as function of E_γ and $-t$ for a t-slope of 1.4 GeV^{-2}.

(b) J/ψ MC yields as function of E_γ and $-t$ for a t-slope of 2.9 GeV^{-2}.

FIG. 48

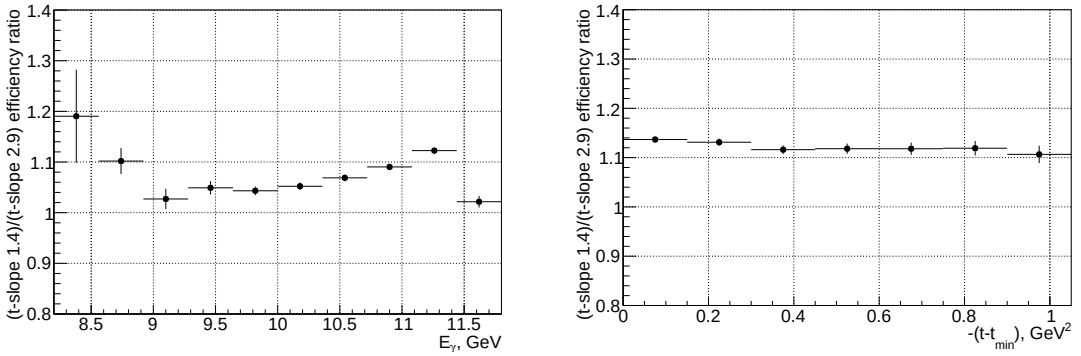

(a) vs beam energy.

(b) vs $-(t - t_{min})$

FIG. 49: Efficiency ratios for t-slopes 1.4 to 2.9 GeV^{-2}.

J/ψ cross-section will affect the efficiencies in both projections, E_γ and t. We have studied the efficiencies for several different t-slopes between 1.4 and 2.9 GeV^{-2}, representing a conservative range choice. While the lower value is close to the lower limit of our measurements (Section IV C), 2.9 GeV^{-2} comes from the SLAC measurement at 19 GeV. In Figs.48a and 48b we plot the MC yields for the two slopes. In Figs.49a and 49b we plot the ratios of the efficiencies for the two slopes in bins of E_γ and $(t - t_{min})$. The ratios can be understood from the 2d-efficiency in Fig.47 convoluted with the distributions in Figs.48a and 48b for the two slopes. In Fig.50 we plot the ratios of the efficiencies for the two t-slopes. Based on our result (Section IV C) one can reduce the range of the input t-slope parameter down to the statistical error, ± 0.347, that range will reduce the variation of the extracted slope. Assuming a linear change of the cross-section within the $1.4 - 2.9$ range, we scale ratios in

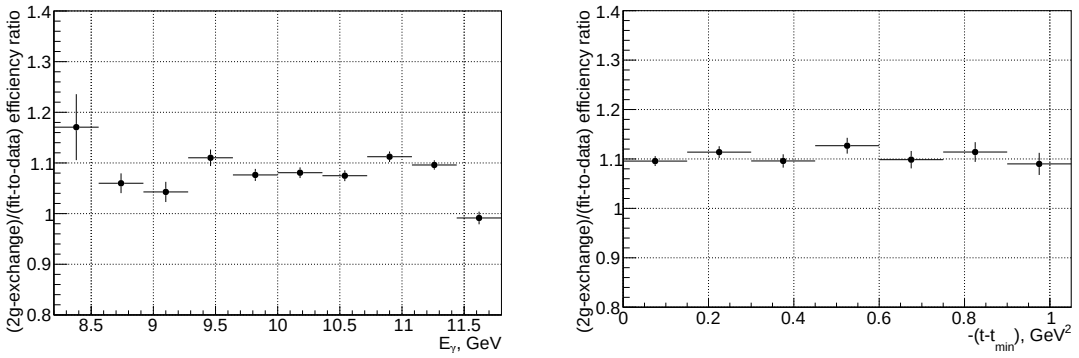

(a) vs beam energy.

(b) vs $-(t - t_{min})$

FIG. 50: Efficiency ratios for the two energy dependencies considered: two-gluon exchange and fit-to-data.

Fig.49a by 0.347/1.5 and treat them as point-by-point relative systematic errors.

Similarly, we have varied the energy dependence of the J/ψ cross-section in MC. We have used the two-gluon exchange cross-section shape from [11] and the shape extracted from our data. The change of the efficiencies is demonstrated in Figs.50a and 50b. The difference (point-by-point) in the cross-section for these two cases, scaled to 20% uncertainty, was used to estimate the effect of the MC cross-section energy dependence.

The relative point-to-point systematical errors from different sources as discussed above are illustrated in Fig.51.

4. P.t.p. systematics for differential cross-section

We have repeated the same procedures to estimate the p.t.p. systematics for the differential cross-section in bins of $(t - t_{min})$. Since in this case we are not using the BH process for normalization, we have included only the uncertainties in the J/ψ fitting method and in the cross-section dependence on the beam energy and the t-slope. The relative point-to-point systematical errors from these sources are illustrated in Fig.52. The errors are dominated by the variations in the J/ψ fitting procedure. We estimated also the effect of these variations on the extracted t-slope as an R.M.S. of the slopes obtained with different J/ψ fitting methods, which is 0.079 GeV^2.

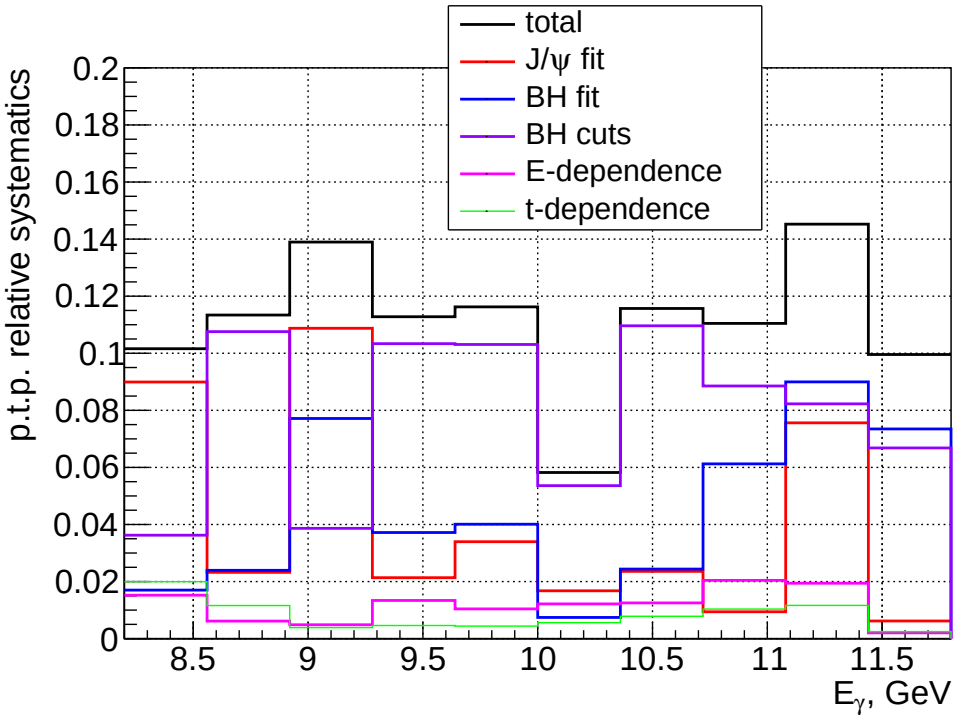

FIG. 51: Relative point-to-point systematical errors from different sources for the total cross-section in bins of beam energy.

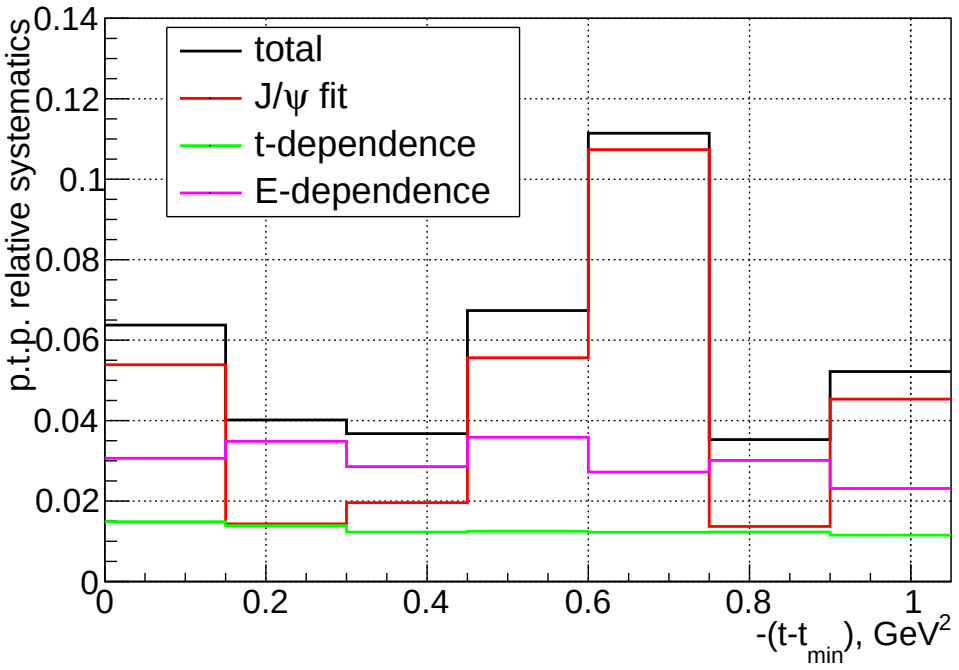

FIG. 52: Relative point-to-point systematical errors from different sources for the differential cross-section in bins of $-(t - t_{min})$.

Method	Related terms	Estimate, %
MC vs data tracking efficiency	$\varepsilon_{BH}/\varepsilon_{J/\psi}$	23
Radiative corrections	$\sigma_{J/\psi}/\sigma_{BH}$	8.3
TCS cross-section contribution	σ_{BH}	8
ρ' contribution: $1.2-2.0$ vs $2-2.5$ BH range	N_{BH}	7
total		26.7

TABLE VI: Systematic errors

bin, GeV	J/ψ fit	BH fit	BH ranges	t-slope	E_γ-dependence
8.2-8.56	0.01050	0.00187	0.00373	0.00152	0.00201
8.56-8.92	0.00828	0.00841	0.03210	0.00204	0.00393
8.92-9.28	0.02860	0.02299	0.01113	0.00139	0.00110
9.28-9.64	0.01742	0.02926	0.07321	0.01000	0.00333
9.64-10	0.02940	0.03425	0.09579	0.00839	0.00347
10-10.36	0.01536	0.00683	0.04694	0.01067	0.00484
10.36-10.72	0.03076	0.03292	0.12700	0.01583	0.00988
10.72-11.08	0.01162	0.07712	0.10978	0.02356	0.01183
11.08-11.44	0.14539	0.200110	0.19377	0.03893	0.02343
11.44-11.8	0.02006	0.238711	0.21846	0.00654	0.00813

TABLE VII: Point-to-point systematic errors from different sources for the total cross-section in bins of beam energy.

H. Summary

The sources and the values of total systematic errors that are under discussions are summarized in Table VI.

Summary of the point-to-point systematic errors for the total cross-section are shown in Table VII.

The J/ψ total cross-section results vs beam energy, the statistical, and point-to-point systematic errors are shown in Table VIII.

Summary of the point-to-point systematic errors for the differential cross-section are shown in Table IX.

The J/ψ differential cross-section results vs $-(t-t_{min})$, the statistical, and point-to-point systematic errors are shown in Table X.

The result for the t-slope is $1.665 \pm 0.347 \pm 0.079$, where the first error is statistical and the second one systematical.

Energy bin, GeV	σ,nb	stat error	p.t.p. syst.
8.2-8.56	0.11592	0.03140	0.01158
8.56-8.92	0.34317	0.06667	0.03448
8.92-9.28	0.31308	0.12709	0.03839
9.28-9.64	0.83483	0.19420	0.08143
9.64-10	0.86836	0.19636	0.10628
10-10.36	0.94905	0.18733	0.05122
10.36-10.72	1.38315	0.28426	0.13604
10.72-11.08	1.27357	0.20634	0.13722
11.08-11.44	2.15758	0.42126	0.31749
11.44-11.8	3.24452	0.92849	0.32437

TABLE VIII: Total cross-section, statistical and point-to-point systematic errors in bins of beam energy. Note a total normalization uncertainty for the cross-section of 26.7%.

bin, GeV^2	J/ψ fit	t-slope	E_γ-dependence
0-0.15	0.02395	0.00742	0.01500
0.15-0.3	0.00516	0.00524	0.01309
0.3-0.45	0.00619	0.00407	0.00939
0.45-0.6	0.01035	0.00232	0.00671
0.6-0.75	0.02079	0.00224	0.004950
0.75-0.9	0.00181	0.00174	0.00426
0.9-1.05	0.00513	0.00143	0.00286

TABLE IX: Point-to-point systematic errors from different sources for the differential cross-section in bins of $-(t-t_{min})$

$-(t-t_{min})$ bin, GeV^2	$d\sigma/dt$,nb/GeV^2	stat error	p.t.p. syst.
0-0.15	1.64311	0.33380	0.02922
0.15-0.3	1.24903	0.26483	0.01501
0.3-0.45	1.08834	0.24788	0.01196
0.45-0.6	0.62749	0.18202	0.01255
0.6-0.75	0.59858	0.16282	0.02148
0.75-0.9	0.46977	0.14484	0.00495
0.9-1.05	0.39982	0.13441	0.00604

TABLE X: Differential cross-sections, statistical and point-to-point systematic errors in bins of $-(t-t_{min})$. Note a total normalization uncertainty for the cross-section of 26.7%.

TABLE XI: Analogy between electro-magnetic and gluonic form factors

	e.m. FF	gluonic FF
reaction	$ep \to ep$	$J/\psi p \to J/\psi p$
transverse size of probe	0	$<<\ 1\ fm$
effective mass scale m_0	0.84 GeV (vector meson)	$\sim 1.1\ GeV$ (two-gluon mass)

VI. INTERPRETATION OF THE RESULTS

The J/ψ photoproduction in the near threshold region is poorly covered by previous experiments [5, 6], while our measurements are the first that extend close to the threshold. This reaction has recently gained significant interest due to its direct relation to the two pentaquarks, $P_c^+(4380)$ and $P_c^+(4450)$, reported by LHCb [12] in their decay into $J/\psi p$. Several groups [13–15] immediately realized that by time-inverting the pentaquark decay and adding a conversion of the beam photon into a $c\bar{c}$ pair based on the VMD model, the existence of these resonances implies they have to be seen in s-channel J/ψ photoproduction: $\gamma p \to P_c^+ \to J/\psi p$ at $E_\gamma \sim 10$ GeV. The only unknown parameter in such a mechanism is the branching fraction of the pentaquark decay into $J/\psi p$.

The near threshold charmonium exclusive production is an excellent probe to study the color charge distribution of the proton, which is another important aspect of these measurements. The heavy quark J/ψ interacts with the light quarks of the proton by exchanging gluons. In [11] based on the dimensional scaling, two- and three-gluon exchange mechanisms near threshold are discussed. In [16] it is argued that the t-dependence of the exclusive reaction is defined by the proton gluonic form-factor for which, in analogy with the electro-magnetic form factors (see Table XI), we can assume a dipole form:

$$F(t)\ \sim\ 1/(1 - t/m_0^2)^2 \tag{7}$$

Generally, there are four gluon form-factors as defined by [17], A_g, B_g, C_g, $\bar{C}_g$, coming from the parametrization of the QCD energy-momentum tensor, $\langle P|T^{\mu\nu}|P'\rangle$, where P and P' are the initial and final proton states.

According to [18] the J/ψ photoproduction near threshold is dominated by the real part

of the $J/\psi p$ elastic amplitude, which is critically important since it contains a term (trace anomaly) related to the fraction of the nucleon mass arising from gluons. In the definitions of [17], this term is related to the C form-factors. In [19] the gluon contribution to the mass of the proton was studied using some assumptions about the gluon form factors. It was found that the J/ψ photoproduction is most sensitive to this contribution in the near threshold region.

A. t-dependence

In Fig.27 we showed the differential cross-section as function of $-(t - t_{min})$ for beam energies in the $10 - 11.8$ GeV region. The strong variation of t_{min} at low energies does not allow us to include the low energy region in this analysis. We obtain a t-slope of $1.665 \pm 0.347 \pm 0.079$ GeV^{-2}, to be compared with the Cornell result [5] at $E_\gamma = 11$ GeV of 1.25 ± 0.2 GeV^{-2} and the SLAC result [6] at $E_\gamma = 19$ GeV of 2.9 ± 0.3 GeV^{-2}. In Fig.53 we test the hypothesis [16] for a dipole t-dependence of the differential cross-section where in addition to the data used in [16] we have added our preliminary results. The beam energies of the different measurements and, correspondingly, the absolute cross-sections vary significantly. In order to compare only the slopes, we have normalized them together and fitted each set individually with exponential functions. A global fit using Eq.7 results in a two-gluon mass parameter of $m_{2g} = 1.14$ GeV. Thus, Fig.53 justifies the use of a form-factor-like dipole t-dependence and illustrates that the change of the t-slope with the beam energy can be explained by the change of t_{min} and the t-range of the different measurements.

In fact the t-dependence is defined by balance of the four form-factors and some kinematical factors. The proton gluon form factors, A_g, B_g, C_g, have been recently calculated on lattice [21]. Interestingly, the A_g form-factor looks very similar to the results on Fig.53; it has been fitted with the dipole function, Eq.(7), resulting in $m_0 = 1.13(6)$, very close to the results of our fit. This might be a coincidence, or it might be that the A form-factor is the dominant one.

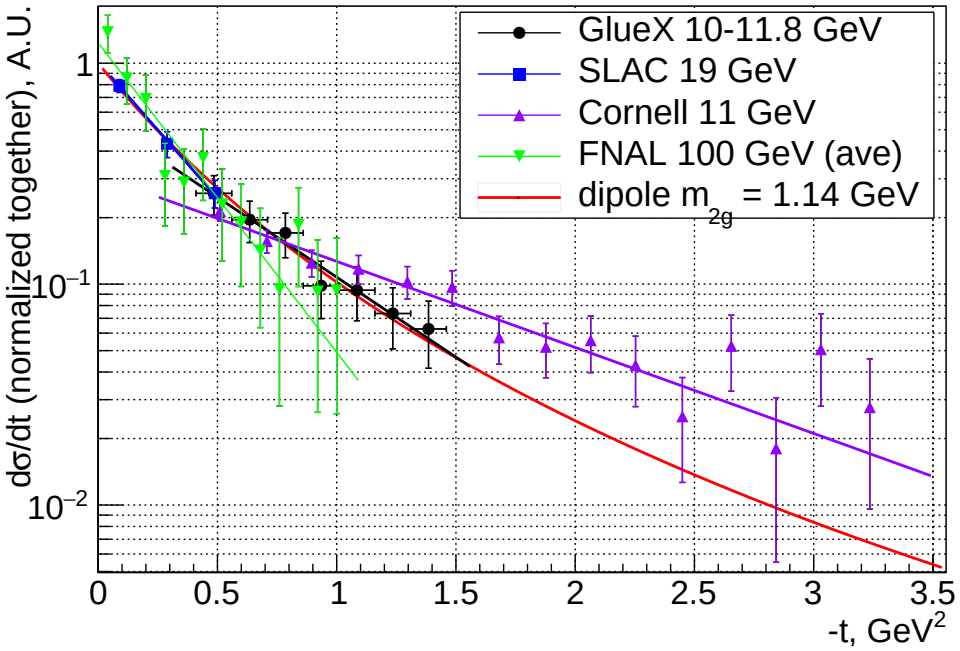

FIG. 53: $d\sigma/dt$ normalized together from experiments with different beam energies: FNAL[20] 100 GeV (average), SLAC 19 GeV, Cornell 11 GeV, GlueX $10-11.8$ GeV. Red curve – Eq.7 with $m_0 = 1.14$ GeV.

B. Beam energy dependence

The GlueX total cross-section in bins of beam energy is shown in Fig.54. In the same figure the Cornell [5] and SLAC [6] measurements are plotted. Note that the SLAC experiment measured $d\sigma/dt$ at $t = t_{min}$. In order to estimate the total cross-section, we have integrated over t assuming the dipole t-dependence from Fig.53. According to the dimensional scaling calculations [11] the differential elastic cross-section is proportional to:

$$\frac{d\sigma}{dt} \sim (1-x)^{2n_s} F^2(t)(s-m_p^2)^2, \tag{8}$$

where n_s is the number of spectators (1 in case of two-gluon and 0 for three-gluon exchange), and x is defined as $(2m_pM_{J/\psi} + M_{J/\psi}^2)/(s-m_p^2)$. Note that $x \to 1$ when approaching the threshold. For the gluonic from-factor $F(t)$ we are using again the dipole form Eq.(7) with $m_0 = 1.14$ GeV. This is in contrast to the paper [11] where they have assumed a simple exponential dependence $F^2 = exp(1.13t)$ based on the old Cornell results [5]. These calculations predict only the shapes of the energy dependence of the cross-section for two-

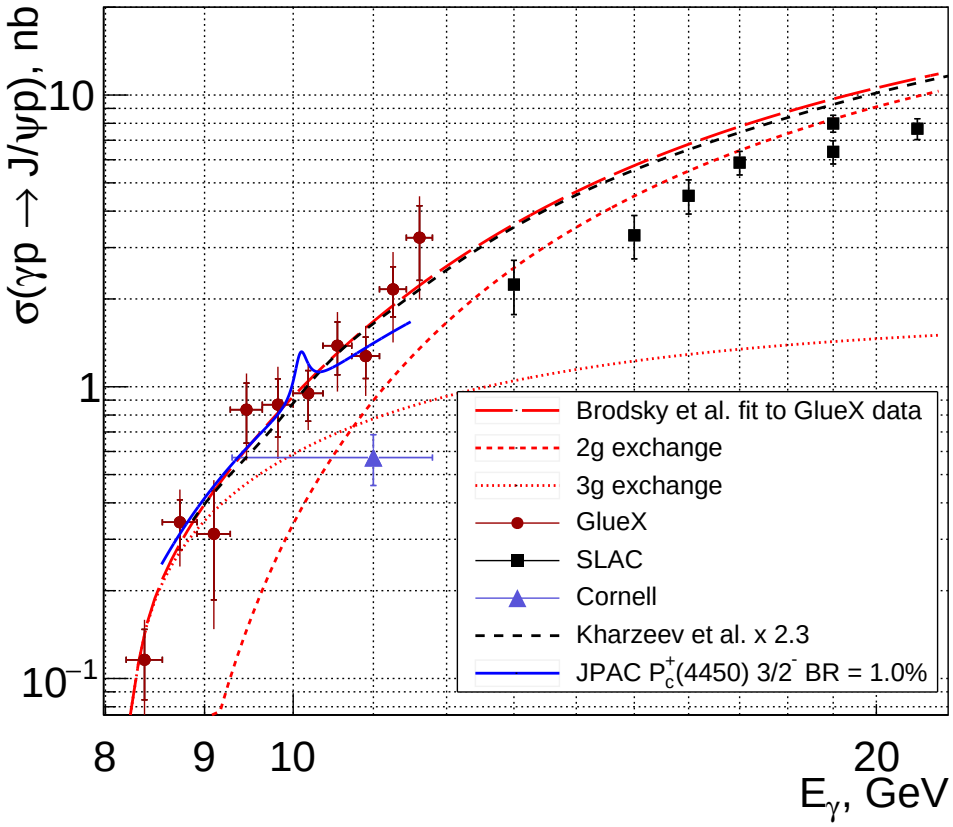

FIG. 54: GlueX results for the J/ψ total cross-section vs beam energy, compared to the Cornell [5] and SLAC [6] results and also to the theoretical predictions [11, 18], and JPAC model [15] correspoding to the upper limit of $\mathcal{B}(P_c^+(4450) \to J/\psi p) = 1.01\%$ for spin-3/2 case as discussed in the text.

or three-gluon exchange. We have used these two curves with two normalization factors as parameters to fit the GlueX data points. One can see (Fig.54) that the three-gluon exchange starts dominating below ~ 11 GeV when approaching the threshold. This is expected since at threshold all the constituents should participate in the reaction. We have plotted also the theoretical curve from [18] multiplied by a factor of 2.3 to fit our data. These are absolute calculations, however according to the authors, there is up to a factor of three uncertainty in the normalization. As long as these calculations are correct they predict the fraction of the nucleon mass arising from gluons to be as high as $\sim 80\%$.

The GlueX total cross-section is a factor of ~ 3 above the Cornell [5] result. It is also a factor of ~ 1.5 above the SLAC [6] cross-section if compared to the Brodsky curve fitted to the GlueX data. Note that the Cornell measurements were done on Be target and the SLAC

ones on deuterium. In both experiments the result was scaled to a nucleon target assuming A^1 dependence. In the SLAC experiment the J/ψ has been registered using both e^+e^- and $\mu^+\mu^-$ decay modes. The two leptons were identified in spectrometers set to different kinematics: scanning the beam energies at $t = t_{min}$ and at several t values for $E_\gamma = 19$ GeV. The SLAC experiment claims systematic uncertainty of 15% dominated by the radiative corrections for electrons and acceptance uncertainties for both lepton types. The Cornell experiments used two electro-magnetic calorimeters to register the electron and positron from the J/ψ decay. There is no estimation of the systematic uncertainty for the Cornell experiment. In both experiments the recoil was not registered.

C. Upper limit on the $P_c^+(4450) \to J/\psi p$ branching fraction

Since the LHCb pentaquark P_c^+ states are produced in the s-channel, they should show up as peaks at $E_\gamma \sim 10$ GeV in the cross section in Fig.54. We see no evidence for such peaks, although the $P_c^+(4380)$ has a large width of ~ 1 GeV in E_γ, and we have little sensitive to its production with the current precision of our data. We set upper limits on $\mathcal{B}(P_c^+(4450) \to J/\psi p)$ by fitting our data with a variation of the model described in [15] where the non-resonant component is described by a combination of Pomeron and tensor amplitudes, in analogy to the two-gluon and three-gluon amplitudes described above. The upper limits at 90% confidence level determined by integrating the likelihood curve of the model fit, are 1.01% and 0.18%, assuming the $P_c^+(4450)$ is spin-3/2 or spin-5/2, respectively. The spin-3/2 case is plotted on Fig.54. A less model-dependent limit is found using the incoherent sum of a Breit-Wigner and the non-resonant component as desribed above. Applying the same likelihood procedure yields an upper limit at 90% confidence level of $\sigma(\gamma p \to P_c^+(4450)) \times \mathcal{B}(P_c^+(4450) \to J/\psi p) < 0.65$ nb.

VII. APPENDIX: TECHNICAL NOTES

A. Data set and software versions

The version of *recon* recon-2017_01-ver03_hdr was used for the data reconstruction. The version of *sim* halld_sim-3.2.0r̂econ17-v3 was used for the MC reconstruction.

List of the 2016 spring runs used in the analysis:

010391	010591	010707	010777	010875	011088	011159	011276	011435	011481	011617
010392	010592	010720	010778	010876	011095	011160	011277	011436	011482	011618
010394	010595	010724	010779	010895	011100	011161	011295	011437	011483	011619
010395	010597	010727	010780	010897	011101	011162	011300	011445	011484	011620
010396	010598	010729	010781	010906	011104	011216	011301	011446	011497	011621
010399	010608	010731	010782	010907	011106	011217	011302	011447	011508	011623
010434	010615	010733	010783	010911	011107	011218	011312	011448	011510	011625
010435	010634	010735	010833	010913	011108	011219	011366	011449	011511	011626
010436	010646	010737	010837	011059	011109	011261	011367	011450	011512	011644
010437	010657	010743	010838	011060	011127	011262	011384	011452	011513	011645
010438	010659	010746	010839	011063	011128	011263	011404	011453	011514	011648
010439	010680	010748	010840	011064	011132	011264	011405	011454	011519	011649
010456	010681	010749	010841	011065	011140	011265	011406	011455	011520	011650
010464	010685	010750	010842	011067	011141	011266	011407	011457	011521	011651
010465	010686	010752	010843	011068	011143	011267	011429	011458	011529	011657
010491	010687	010753	010844	011078	011145	011269	011430	011473	011532	011658
010492	010691	010755	010845	011082	011150	011270	011431	011474	011553	011659
010497	010693	010758	010867	011084	011156	011272	011432	011475	011554	011663
010498	010703	010765	010871	011086	011157	011273	011433	011476	011555	
010590	010704	010768	010873	011087	011158	011275	011434	011477	011569	

List of the 2017 spring runs used in the analysis:

030274	030350	030431	030474	030590	030636	030682	030769	030826	030902	030995

030276	030351	030432	030477	030591	030637	030684	030770	030827	030903	030996
030277	030352	030433	030480	030592	030638	030686	030778	030829	030920	030998
030279	030355	030434	030481	030593	030639	030687	030779	030830	030923	030999
030280	030361	030436	030482	030595	030641	030688	030780	030833	030924	031000
030281	030380	030437	030484	030596	030642	030690	030783	030834	030926	031001
030282	030381	030441	030485	030597	030643	030693	030784	030835	030927	031002
030283	030383	030442	030486	030598	030648	030694	030785	030836	030928	031003
030284	030384	030446	030487	030600	030649	030695	030787	030838	030929	031004
030285	030385	030447	030488	030602	030650	030696	030788	030839	030930	031005
030286	030386	030448	030489	030607	030651	030697	030796	030840	030947	031018
030298	030387	030449	030490	030608	030652	030698	030797	030841	030951	031023
030299	030388	030450	030493	030610	030653	030699	030800	030842	030952	031029
030300	030389	030451	030494	030611	030654	030701	030801	030843	030953	031031
030320	030390	030452	030495	030612	030655	030730	030802	030844	030954	031032
030321	030401	030453	030496	030614	030656	030731	030803	030847	030955	031034
030322	030402	030454	030497	030616	030657	030732	030804	030848	030956	031036
030323	030403	030455	030499	030618	030658	030733	030805	030855	030957	031046
030324	030404	030459	030567	030620	030659	030734	030807	030856	030958	031049
030326	030405	030460	030568	030621	030660	030735	030808	030857	030959	031050
030327	030406	030461	030570	030622	030666	030736	030809	030858	030961	031051
030329	030407	030462	030571	030623	030667	030737	030810	030859	030962	031052
030330	030408	030463	030575	030624	030668	030738	030811	030888	030963	031053
030331	030409	030464	030577	030625	030672	030739	030812	030889	030964	031054
030332	030410	030465	030578	030626	030673	030740	030813	030890	030965	031055
030343	030411	030466	030579	030627	030674	030741	030815	030891	030966	031056
030344	030420	030467	030580	030629	030675	030742	030816	030893	030980	031057
030345	030421	030468	030581	030630	030676	030743	030818	030895	030981	
030346	030422	030469	030582	030632	030677	030744	030821	030896	030982	
030347	030424	030470	030586	030633	030678	030745	030822	030898	030992	
030348	030428	030471	030587	030634	030679	030749	030823	030899	030993	
030349	030429	030473	030589	030635	030680	030754	030824	030900	030994	

variable	units	lower limit	upper limit
M^2_{miss}	GeV^2	-0.25	0.25
Pt_{miss}	GeV	n/a	0.5
E/p (kin.fit.)		0.7	n/a
extra charged tracks	#	0	6
neutrals	#	0	12
e^+/e^- $abs\Delta t$ in TOF	ns	0	1
e^+/e^- $abs\Delta t$ in BCAL	ns	0	2.5
e^+/e^- $abs\Delta t$ in FCAL	ns	0	2.5
π^+/π^- $abs\Delta t$ in TOF	ns	0	2
π^+/π^- $abs\Delta t$ in BCAL	ns	0	2.5
π^+/π^- $abs\Delta t$ in FCAL	ns	0	2.5
K^+/K^- $abs\Delta t$ in TOF	ns	0	0.75
K^+/K^- $abs\Delta t$ in BCAL	ns	0	2.5
K^+/K^- $abs\Delta t$ in FCAL	ns	0	2
p^+/p^- $abs\Delta t$ in TOF	ns	0	2.5
p^+/p^- $abs\Delta t$ in BCAL	ns	0	2.5
p^+/p^- $abs\Delta t$ in FCAL	ns	0	2.5
γ $abs\Delta t$ in BCAL	ns	0	1.5
γ $abs\Delta t$ in FCAL	ns	0	2.5

TABLE XII: Analysis cuts that have been modified from the standard values.

variable	units	lower limit	upper limit
e^+/e^- BCAL p/E		0.8413	1.1827
e^+/e^- FCAL p/E		0.9562	1.1521
e^+/e^- $\mathrm{BCAL}_{pre}\sin\theta$	GeV	0.03	n/a
e^+/e^- θ	deg	2	n/a
e^+/e^- p	GeV	0.4	n/a
p p	GeV	0.4	n/a
Kin. fit χ^2		> 0	5000

TABLE XIII: Additional cuts applied in custom analysis.

B. Summary of the cuts

The exclusive reaction 2 is identified using the DReaction factory (from DAnalysis library) using the cuts in Table XII. Kinematic fit was requested using both $p4$ and vertex constraints.

The additional cuts applied in the custom analysis are summarized in Table XIII.

[1] J. Ballam, G. Chadwick, Y. Eisenberg, E. Kogan, K. Moffeit, P. Seyboth, I. Skillicorn, H. Spitzer, and G. Wolf, Eur.Phys.J.C **23**, 675 (1973).

[2] R. Paremuzyan, private communication (2017).

[3] E. Berger, M. Diehl, and B. Pire, Eur.Phys.J.C **23**, 675 (2002).

[4] R. Jones, private communication (2018).

[5] B. Gittelman, K. M. Hanson, D. Larson, E. Loh, A. Silverman, and G. Theodosiou, Phys. Rev. Lett. **35**, 1616 (1975).

[6] U. Camerini, J. Learned, R. Prepost, C. Spencer, D. Wiser, W. Ash, R. L. Anderson, D. M. Ritson, D. Sherden, and C. K. Sinclair, Phys. Rev. Lett. **35**, 483 (1975).

[7] A. Schertz, private communication (2019).

[8] E. Barberio et al. , Comput.Phys.Commun. **79**, 291 (1994).

[9] M. Heller, O. Tomalak, and M. Vanderhaeghen, Phys. Rev. D **97**, 076012 (2018).

[10] M. Boer, private communication and report on the meeting (2019).

[11] S. Brodsky, E. Chudakov, P. Hoyer, and J. Laget, Phys. Lett. B **498**, 23 (2001).

[12] R. Aaij et al. (LHCb collaboration), Phys. Rev. Lett. **115**, 072001 (2015).

[13] V. Kubarovsky and M. B. Voloshin, Phys. Rev. D **92**, 031502 (2015).

[14] M. Karliner and J. Rosner, Phys. Lett. B **752**, 329 (2016).

[15] A. Blin, C. Fernandez - Ramirez, A. Jackura, V. Mathieu, V. Mokeev, A. Pilloni, and A. Szczepaniak, Phys. Rev. D **94**, 034002 (2016).

[16] L. Frankfurt and M. Strikman, Phys. Rev. D **66**, 031502 (2002).

[17] X. Ji, Phys. Rev. Lett. **78**, 610 (1997).

[18] D. Kharzeev, H. Satz, A. Syamtomov, and G. Zinovev, Nucl.Phys. A **661**, 568 (1999).

[19] Y. Hatta and D.-L. Yang, //arxiv.org/pdf/1808.02163.pdf (2018).

[20] M. Binkley, C. Bohler, J. Butler, J. Cumalat, I. Gaines, M. Gormley, D. Harding, R. Loveless, and J. Peoples, Phys. Rev. Lett. **48**, 73 (1982).

[21] P. E. Shanahan and W. Detmold, https://arxiv.org/pdf/1810.04626.pdf.

[22] A. Sibitsev, S. Krewald, and A. Thomas, J. Phys. G **30**, 1427 (2004).

[23] A. Sibitsev, S. Krewald, and A. Thomas, nucl-th/0310021 (2003).